



**TRIBHUVAN UNIVERSITY
INSTITUTE OF ENGINEERING
THAPATHALI CAMPUS**

**MAJOR PROJECT REPORT
on
DESIGN AND DEVELOPMENT OF CYCLOROTOR FOR PARAMETRIC
STUDY OF THRUST VECTORING**

Submitted By:

Abhishek Kandel (THA075BME003)

Milan Dhami (THA075BME019)

Ringjing Tamang (THA075BME030)

Rohit Pati (THA075BME031)

Submitted To:

**DEPARTMENT OF AUTOMOBILE AND MECHANICAL ENGINEERING
THAPATHALI CAMPUS
KATHMANDU, NEPAL**

March 2023



**TRIBHUVAN UNIVERSITY
INSTITUTE OF ENGINEERING
THAPATHALI CAMPUS**

**MAJOR PROJECT REPORT
on
DESIGN AND DEVELOPMENT OF CYCLOROTOR FOR PARAMETRIC
STUDY OF THRUST VECTORING**

Submitted By:

Abhishek Kandel (THA075BME003)

Milan Dhami (THA075BME019)

Ringjing Tamang (THA075BME030)

Rohit Pati (THA075BME031)

Submitted To:

DEPARTMENT OF AUTOMOBILE AND MECHANICAL ENGINEERING
THAPATHALI CAMPUS
KATHMANDU, NEPAL

March 2023



**TRIBHUVAN UNIVERSITY
INSTITUTE OF ENGINEERING
THAPATHALI CAMPUS**

MAJOR PROJECT REPORT

on

**DESIGN AND DEVELOPMENT OF CYCLOROTOR FOR PARAMETRIC
STUDY OF THRUST VECTORING**

Submitted By:

Abhishek Kandel (THA075BME003)

Milan Dhami (THA075BME019)

Ringjing Tamang (THA075BME030)

Rohit Pati (THA075BME031)

Submitted To:

**DEPARTMENT OF AUTOMOBILE AND MECHANICAL ENGINEERING
THAPATHALI CAMPUS, KATHMANDU, NEPAL**

In the partial fulfillment of the award of the Bachelor's Degree in Mechanical
Engineering

Under the Supervision of

Er. Biman Rimal

March 2023

COPYRIGHT

The author has agreed that the library, Department of Automobile and Mechanical Engineering, Thapathali Campus, Institute of Engineering may make this project report freely available for inspection and study. Moreover, the author has agreed that permission for extensive copying of this project report for scholarly purposes may be granted by the professor who supervised the project work recorded herein or, in their absence, by the Head of the Department wherein the project report was done. It is understood that recognition will be given to the author of this report and to the Department of Automobile and Mechanical Engineering, Thapathali Campus, Institute of Engineering, in any use of the material of this project report.

Copying or publication or other illegal and immoral use of this report for financial gain without the approval of the Department of Automobile and Mechanical Engineering, Thapathali Campus Institute of Engineering and author's written permission is strictly prohibited.

Request for permission to copy or to make any other use of the material in this report, in whole or in part, should be addressed to:

Head

Department of Automobile and Mechanical Engineering

Thapathali Campus, Institute of Engineering

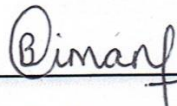
Thapathali, Kathmandu

Nepal



CERTIFICATE OF APPROVAL

The undersigned certify that they have read and recommended to the **Department of Automobile and Mechanical Engineering, IOE, Thapathali Campus**, a major project work entitled “**Design and Development of Cyclorotor for Parametric Study of Thrust Vectoring**” submitted by **Abhishek Kandel, Milan Dhimi, Ringjing Tamang** and **Rohit Pati** in partial fulfillment for the award of Bachelor’s Degree in Mechanical Engineering. The Project was carried out under special supervision and within the time frame prescribed by the syllabus.



Supervisor, Er. Biman Rimal

Department of Automobile and Mechanical Engineering
Institute of Engineering, Thapathali Campus



External Examiner, Sudip Bhattarai, Ph.D.

Assistant Professor, Aerospace Engineering
Department of Mechanical and Aerospace Engineering
Institute of Engineering, Pulchowk Campus



Head of Department, Er. Prajwal Raj Shakya

Department of Automobile and Mechanical Engineering
Institute of Engineering, Thapathali Campus

Date: 2023/03/23

ACKNOWLEDGEMENT

We would like to take this opportunity to express the deepest gratitude to our supervisor, Er. Biman Rimal for offering immense support and guidance for the successful accomplishment of this project. We would like to extend our sincere thanks to the Department of Automobile and Mechanical Engineering and IOE Thapathali Campus for providing us with the opportunity to conduct this project. We are also thankful to all the lecturers and faculty who have helped us directly and indirectly on this project.

We would like to extend our gratitude to Mrs. Elena Shrestha, (Postdoctoral Research Fellow at University of Michigan) for providing guidance and suggestions during different phases of our project. We are thankful to Mr. Moble Benedict (Associate Professor, Texas A&M University) for helping us with problems encountered during the experimental phase. We would also like to extend our thanks to Mr. Julian Schliessus (MSc Aerospace, University of Stuttgart) for providing support regarding the CFD simulation on this project.

Abhishek Kandel	(THA075BME003)
Milan Dhami	(THA075BME019)
Ringjing Tamang	(THA075BME030)
Rohit Pati	(THA075BME031)

ABSTRACT

Cyclorotor is a horizontal axis propulsion system with airfoil blades attached between two rotor wheels parallelly to the axis of rotation. The unique feature of this propulsion system is the variable pitching mechanism which offers better maneuverability characteristic for air vehicles. This propulsion system is claimed to produce adequate thrust even at low speed which helps to simplify the rotating mechanism and reduce noise which has widened its scope for use in VTOL aircraft. Research has been going on in this field with the quest of optimizing it for use in air vehicles. It is important to have a better control system for propulsion systems and aircraft to acquire airworthiness. For a better control system of the variable pitching mechanism in a cyclorotor, it is required to have knowledge on the thrust vector pattern. Hence this report discusses the experimental study of thrust vector in cyclorotor where the thrust vector pattern is analyzed with respect to the eccentricity phase angle.

TABLE OF CONTENTS

COPYRIGHT	ii
CERTIFICATE OF APPROVAL	iii
ACKNOWLEDGEMENT	iv
ABSTRACT	v
TABLE OF CONTENTS	vi
LIST OF FIGURES	xi
LIST OF TABLES	xv
LIST OF ABBREVIATIONS	xvi
CHAPTER ONE: INTRODUCTION	1
1.1 BACKGROUND	1
1.2 INTRODUCTION	4
1.3 PROBLEM STATEMENT	5
1.4 PROJECT OBJECTIVES	6
1.4.1 MAIN OBJECTIVE	6
1.4.2 SPECIFIC OBJECTIVES	6
1.5 SCOPES OF CYCLOROTOR	6
CHAPTER TWO: LITERATURE REVIEW	8
CHAPTER THREE: METHODOLOGY	17
3.1 REVIEW OF LITERATURES	17

3.2	OBSERVATION	17
3.3	SOFTWARES EMPLOYED	17
3.3.1	CATIA V5	17
3.3.2	XFLR5	18
3.3.3	OpenFOAM	18
3.4	PROJECT FLOW CHART	20
CHAPTER FOUR: MATHEMATICAL MODELING		21
4.1	AIRFOIL MODELING	21
4.2	CYCLOROTOR	23
4.2.1	KINEMATIC MODEL	24
4.2.2	AERODYNAMIC ANALYSIS	26
4.3	TRANSMISSION GEAR AND BELT	29
4.3.1	GT2 TIMING PULLEY	29
4.3.2	GT2 TIMING BELT	30
4.4	LOAD CELL	31
CHAPTER FIVE: MATERIALS AND COMPONENTS SELECTION		32
5.1	MATERIALS FOR FABRICATION	32
5.1.1	PLA FILAMENT	32
5.1.2	ALUMINUM TUBE	33
5.1.3	CARBON FIBER ROD	34
5.2	COMPONENTS	35

5.2.1	GT2 TIMING BELT	35
5.2.2	1400 KV BRUSHLESS DC (BLDC) MOTOR	35
5.2.3	ELECTRONIC SPEED CONTROLLER (ESC)	36
5.2.4	LITHIUM POLYMER BATTERY	37
5.2.5	SERVO TESTER	38
5.2.6	STEEL BOLTS AND NUTS	38
5.2.7	STEEL MACHINE SCREWS	39
5.2.8	LOAD CELL	40
5.2.9	HX711 MODULE	41
5.2.10	ARDUINO UNO	41
CHAPTER SIX: DESIGN, SIMULAITON AND ANALYSIS		43
6.1	AIRFOIL DESIGN AND ANALYSIS	43
6.2	ROTOR DESIGN	45
6.2.1	ROTOR WHEEL	46
6.2.2	AIRFOIL BLADE	48
6.3	TRANSMISSION DESIGN	51
6.3.1	GEAR DESIGN	51
6.3.2	BELT DESIGN	52
6.4	SIMULATION OF CYCLOROTOR	52
6.4.1	SOLVERS	52
6.4.2	TURBULENCE MODELING	54

6.4.3	THE SST K- ω TURBULENCE MODEL	55
6.4.4	ARBITRARY MESH INTERFACE (AMI)	55
6.4.5	MESHING	55
6.4.6	BOUNDARY CONDITIONS:	58
6.4.7	MOTION OF BLADES	60
6.4.8	SIMULATION	60
6.4.9	POST PROCESSING:	61
	CHAPTER SEVEN: MANUFACTURING AND ASSEMBLY	65
7.1	FABRICATION	65
7.1.1	CYCLOROTOR	65
7.1.1.1	MAIN ROTOR WHEEL	65
7.1.1.2	AIRFOIL BLADE	65
7.1.1.3	CARBON ROD SPAR	66
7.1.1.4	CONTROL ROD	66
7.1.1.5	MAIN ROTOR SEPARATOR SHAFT	67
7.1.1.6	SERVO-SHAFT COUPLER	68
7.1.1.7	PULLEY COUPLER	69
7.1.1.8	TIMING PULLEY	69
7.1.2	TEST RIG	70
7.2	ASSEMBLY	72
7.2.1	CYCLOROTOR	72

7.2.2	EXPERIMENTAL SETUP	73
CHAPTER EIGHT: EXPERIMENTATION, RESULT AND DISCUSSION		75
8.1	EXPERIMENTATION	75
8.2	EXPERIMENTAL RESULTS AND DISCUSSION	77
CHAPTER NINE: CONCLUSION		82
CHAPTER TEN: PROBLEMS AND LIMITATIONS		83
10.1	PROBLEMS	83
10.2	LIMITATIONS OF THE PROJECT	83
REFERENCES		84
APPENDICES		88

LIST OF FIGURES

Figure 1 Sverchkov's Samoljot, St-Peterburg, 1909 (Bowers, 2013)	1
Figure 2 Rohrbach Cyclogyro (Arndt, n.d.).....	2
Figure 3 Cyclorotor model.....	5
Figure 4 Overview of OpenFOAM structures	18
Figure 5 Project flow chart	20
Figure 6 Airfoil nomenclature	21
Figure 7 Center of pressure for an airfoil.....	22
Figure 8 Blade control mechanism schematic	24
Figure 9 Leading and trailing edge coordinates.....	26
Figure 10 Horizontal and vertical resultant force components of blade in hovering state (Leger, Pascoa, & Xisto, 2015).....	27
Figure 11 Analysis of induced velocities (Leger, Pascoa, & Xisto, 2015).....	28
Figure 12 PLA filament spool.....	33
Figure 13 Aluminum tube.....	34
Figure 14 Carbon fiber rod	34
Figure 15 GT2 timing belt	35
Figure 16 1400 KV Brushless DC motor.....	36
Figure 17 30A Electronic Speed Controller.....	37
Figure 18 LiPo Battery 2200 mAh 3S	37
Figure 19 Servo tester	38

Figure 20 Steel machine screw	40
Figure 21 Load cell	40
Figure 22 HX711 Amplifier.....	41
Figure 23 Arduino Uno	42
Figure 24 Coefficient of lift vs angle of attack curve	44
Figure 25 Coefficient of lift vs coefficient of drag curve	44
Figure 26 Rotor wheel tensile stress vulnerable site.....	47
Figure 27 Section of the vulnerable impact site.....	47
Figure 28 Blade force diagram	49
Figure 29 Refined mesh sphere.....	56
Figure 30 Front view of the mesh	57
Figure 31 Zoomed view of the mesh with AMI	57
Figure 32 Force along Y-axis vs phase angle curve	63
Figure 33 Force along X-axis vs phase angle curve	63
Figure 34 Thrust direction vs phase angle curve.	64
Figure 35 Thrust vs phase angle curve.	64
Figure 36 Main rotor wheel	65
Figure 37 NACA0015 Airfoil blade	66
Figure 38 Control rod.....	67
Figure 39 Main rotor separator shaft	67
Figure 40 Servo-shaft coupler (Outboard).....	68

Figure 41 Servo-shaft coupler (Inboard).....	68
Figure 42 Pulley coupler.....	69
Figure 43 GT2 timing pulley 20 teeth.....	69
Figure 44 GT2 timing pulley 60 teeth.....	70
Figure 45 Test rig.....	71
Figure 46 System architecture of test rig	71
Figure 47 Assembled product of cyclorotor.	72
Figure 48 Experimental setup	73
Figure 49 Driveline system architecture	74
Figure 50 Electrical wiring for test rig.....	74
Figure 51 Coordinate system for the whole system (left) coordinate system for phase angle (right).....	76
Figure 52 Force along Y-axis vs phase angle curve	78
Figure 53 Force in X-axis vs phase angle curve	78
Figure 54 Thrust magnitude vs phase angle curve.....	79
Figure 55 Thrust direction vs phase angle curve.	79
Figure 56 Comparison of force in Y-axis & X-axis with phase angle.....	80
Figure 57 Comparison of experimental and numerical forces along Y-axis	80
Figure 58 Comparison of experimental and numerical forces along X-axis	81
Figure 59 Comparison of experimental and numerical thrust results	81
Figure 60 Design Specification of GT2 Tooth Profile.....	88

Figure 61 Shear Force Diagram	88
Figure 62 Bending Moment Diagram	89

LIST OF TABLES

Table 1 Design parameters for the cyclorotor used in this project.	50
Table 2 Statistic inspection of mesh	58
Table 3 Simulation parameters	60
Table 4 Simulation results	62
Table 5 GT2 Timing Belt Specification (Source: https://www.himalayansolution.com/product/200-2gt-6mm-belt)	89
Table 6 Carbon Fiber Properties (Source: https://goodwinds.com/technical-material-specifications/)	90

LIST OF ABBREVIATIONS

2D	Two Dimensional
BLDC	Brushless Direct Current
CBS	Cycloidal Blades System
CFD	Computational Fluid Dynamics
ESC	Electronic Speed Controller
FM	Figure of Merit
GA	Genetic Algorithm
GM	Gradient Method
IAT	Innovation Aeronautics Technologies
MAV	Micro Air Vehicle
PIV	Particle Image Velocimetry
PLA	Polylactic Acid
SOGA	Single-Objective Genetic Algorithm
URANS	Unsteady Reynold-Averaged Navier Stokes
VTOL	Vertical Take Off Landing
mph	miles per hour
PIMPLE	Pressure Implicit Method for Pressure-Linked Equations

CHAPTER ONE

INTRODUCTION

1.1 BACKGROUND

Ideas regarding cyclorotor were present even during the 19th century. In 1909 Russian engineer Sverchkov proposed "Samoljot", also named - "wheel orthopter" which even though is difficult to classify as cyclocopter can be regarded as a proto-cyclocopter. It used 3 flat surfaces and rudder and lift and thrust had to be generated by paddle wheels. It was unsuccessful and couldn't fly (Bowers, 2013).

In Feb 1923, Jonathan Edward Caldwell from US filed an application for a patent covering a "Cyclogyro" that was designed to take off vertically and transit to forward flight. The plane's wings were small airfoil blades mounted in Ferris wheel-like rotating frames protruding from either side of a conventional aircraft fuselage. The "Cyclogyro" patent was granted in the summer of 1927. But this device was too unstable for human flight (Jonathan Edward Caldwell - Wikipedia, 2022).

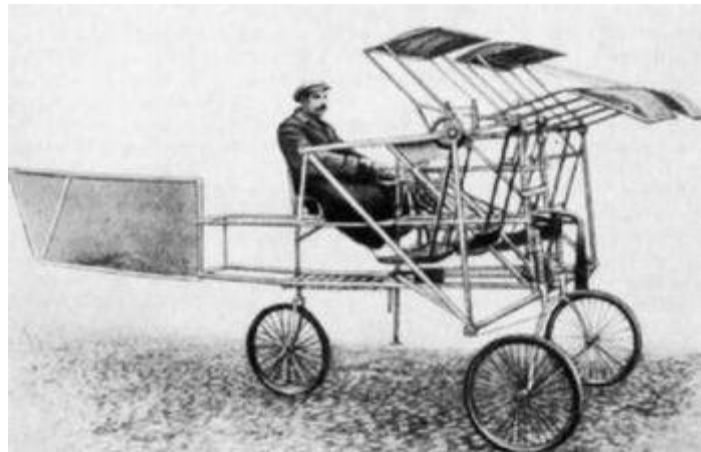


Figure 1 Sverchkov's Samoljot, St-Peterburg, 1909 (Bowers, 2013)

In 1933, experiments in Germany by Adolf Rohrbach resulted in a paddle-wheel wing arrangement. Oscillating winglets went from positive to negative angles of attack during each revolution to create lift, and their eccentric mounting would, in theory, produce nearly any combination of horizontal and vertical (Arndt, n.d.) forces but the

foreign aviation journals of the time casted doubt on the soundness of the design which meant that funding for the project could not be raised.



Figure 2 Rohrbach Cyclogyro (*Arndt, n.d.*)

Also, in 1933 NACA Technical Memorandum No. 727, C. B. Standgren claimed that his pioneer paper to be made public described the theory behind the cyclogyro in any real technical detail. Standgren's analysis described the kinematics of blade movement for a cycloidal rotor. His observations were derived from "numerous tests made at the Institut Aerotechnique de Saint-Cyr, by means of different small-scale models constructed with the cooperation of the Office National de Inventions et de la Societe 'Expansion Franco-Scandinave' relations." He also states that the Liore and Oliver airplane company built a full-scale aircraft. There was no discussion of the actual tests rather Standgren mathematically described the kinematics of the cycloidal rotor and the mechanism by which generated thrust (Standgren, 1933). In the same year an experimental model of the cyclogyro was first presented by John B. Wheatley (Wheatley, Rotating-wing Aircraft Compared to Conventional Airplanes, 1934). In 1934, he and Ray Windley tested a rotor with 4 blades of chord 0.312 ft, and a diameter and wingspan of 8ft. The experiment results showed that the cyclogyro of these dimensions "would be able to ascend vertically, fly horizontally, and glide without power" (Wheatley, Choice of Airfoils for Rotating Wing Aircraft, 1934).

The main problems faced by models until now was the requirement of high strength material. Though the first successful flight was possible by the 1930s it was too unstable and unsafe. Research on the subject was mostly abandoned after World War II, with researchers unable to design a control mechanism suitable for the aircraft, and rotor propeller becoming used for vertical take-off dominantly. The biggest issue in cyclorotors was the fact that blades must take large transverse centrifugal bending loads, and during that time, they did not have the materials that had the strength-to-weight ratio to do that. But modern technology and the use of computational fluid dynamics in vehicle design along with material advancement has made practical prototype development possible.

Even though many attempts were made to build such an aircraft and numerous patents were filed, successful flight of a cycloidal rotor aircraft remained as an impossible feat for nearly a century, until recently when the first cyclocopter was flown at the University of Maryland in 2011 by team of Mobile Benedict and R.Gupta (Jarugumilli, Chopra, & Benedict, 2011) (Benedict, Chopra, & Gupta, Design, Development and Open-Loop Flight-Testig of a Twin-Rotot Cyclocopter, 2013). And further feasibility of this concept was demonstrated here again in 2013 with a quadrotor cyclocopter capable of free hover by Mobile Benedict, Joseph Mullins, and Vikram Hrishikeshavan. This quadrotor had a gross weight of 800 grams and 2 ft by 2 ft by 1.5 ft in dimension (Benedict, Joseph, Chopra, & Gupta, 2016). An untethered model cyclocopter was flown in 2011 at the Northwestern Polytechnic Institute in China.

On the 20th of August 2021, Cyclotech, an Austrian company made a cyclorotor that performed its first free flight and landing with the Cyclorotor technology (CycloTech Home - CycloTech Reovlution of motion, 2021).

Advanced Research Foundation (ARF), the research arm of the Russian Military, is also working on a cyclorotor. ARF concluded after year-long research that the best iteration for a flying vehicle that can carry a load of 220 - 2,200 pounds with passengers is a cyclocopter (Blain, 2021).

1.2 INTRODUCTION

A cyclorotor (cyclogyro, cyclocopter, cycloidal propeller) is a heavier-than-air flight vehicle capable of vertical takeoff and landing using cyclically pitched, horizontal rotor blades. Typical configurations consist of 4 to 6 rotor blades per rotor, which spin parallel to each other around a central axis. As they turn, the rotor blades pivot about their longitudinal axis. The pivot function is periodic, with each rotation about the common axis defining the frequency of the pitching function. Pivot functions resemble a sine curve and function to generate a constant lift, keeping a positive angle of attack in quadrants one and two, and a negative angle of attack in quadrants three and four. However, the pivot functions can be adapted to be more efficient in different flight envelopes, for example during hovering, forward flight, or maneuvering. A key characteristic of a cyclorotor is that it can very rapidly change its pivot function, almost instantly changing direction and magnitude of thrust. Magnitude of thrust is altered by changing the amplitude of the pivot function, and the direction of thrust is changed by shifting the phase of the pivot function. Cycloidal rotors are a viable means to produce aerodynamic forces whose direction can be rapidly varied 360° in a plane normal to the axis of rotation. The superposition of two blade motions generates the thrust. For one motion, the blades rotate about the rotor center while maintaining their span axes always parallel to the axis of the central drum. For the other motion, the blades individually pitch about their own pivoting axis with the same frequency as the main rotation. Changing the phase delay or the magnitude of their pitching motion allows almost instant thrust direction adjustments. The most frequent means to impose the pitching motion to the blades is with rigid links. The central offset of these links generates the cyclic pitching motion of the blades.

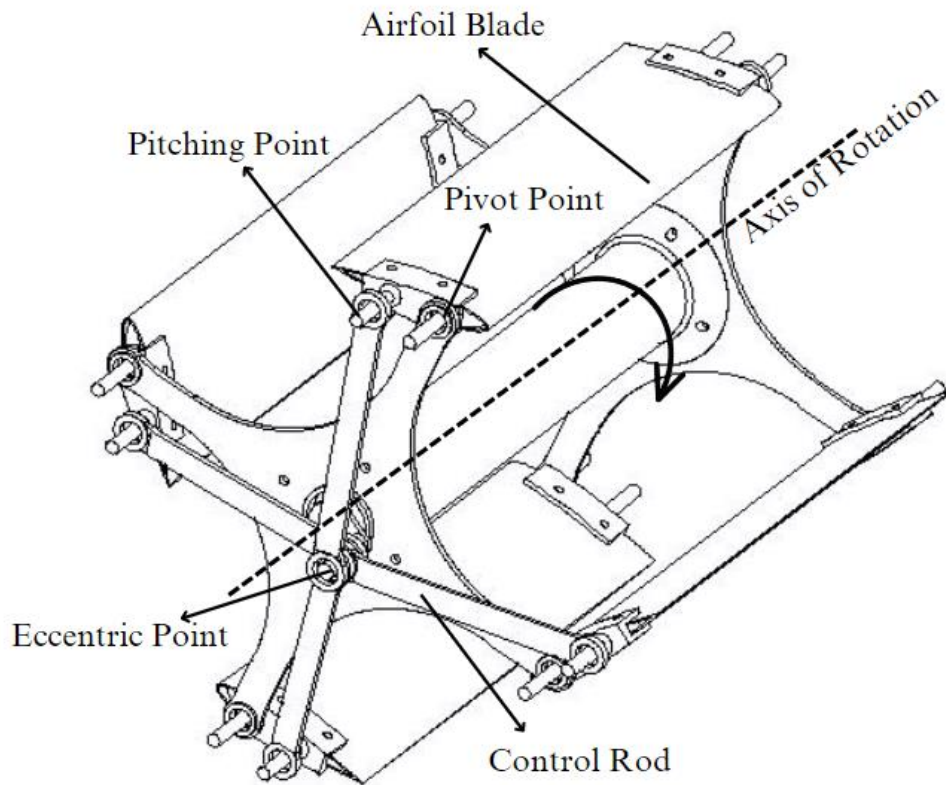


Figure 3 Cyclorotor model

1.3 PROBLEM STATEMENT

Concept of cyclorotor dates to the time when different innovations and experiments on aviation were carried out before airplanes and helicopters were fully realized; however due to low strength to weight ratio materials this concept was considered unviable. With the advent of time and development of high strength to weight ratio materials this concept has been brought back to research. Research has been carried out on control mechanisms, optimization of the mechanism and its feasibility to be used on aircraft propulsion. Different optimization techniques and different analysis methods had been used to model the best performing cyclorotor. Besides the efforts being made it has been very hard for the researchers to gain stable and controlled flight with this propulsion system. The cyclorotor features a variable pitching mechanism which allows the blades to pitch while it is rotating about the central rotational axis. This unique feature of the cyclorotor enables thrust vectoring which can aid the aircraft to gain better

maneuverability. Besides the fact that the thrust vectoring analytical model plays a significant role in flight performance of the cyclorotor, more research has been carried out on other than this specific portion of the cyclorotor. Therefore, we intend to develop a cyclorotor model and conduct a parametric study on it with an objective to obtain the thrust vectoring patterns with respect to the eccentricity phase angle which is the sole responsible parameter for the thrust vectoring.

1.4 PROJECT OBJECTIVES

The main object of this project is to experimentally study the thrust vector pattern generated due to the variation in eccentricity phase angle.

1.4.1 MAIN OBJECTIVE

- To design, build and study the thrust vectoring pattern in cyclorotor.

1.4.2 SPECIFIC OBJECTIVES

- To design and build a cyclorotor.
- To design and fabricate a thrust test rig.
- To conduct an experimental study on thrust vectoring pattern in cyclorotor.

1.5 SCOPES OF CYCLOROTOR

When compared to a conventional edgewise rotor at the same disk loading (thrust/disk area), an optimized cyclorotor has a higher power loading (thrust/power) in hover. Since all spanwise blade sections of the cyclorotor operate under similar aerodynamic conditions, the blades can be optimized to achieve best aerodynamic efficiency. In addition, the uniform spanwise distribution of aerodynamic forces enables the cyclorotor to operate at lower tip speeds, thereby improving the acoustics signature. Previous PIV studies have also shown the existence of beneficial unsteady aerodynamic mechanisms, such as leading-edge vortices that delay the onset of blade stall and improve the lift producing capability and aerodynamic efficiency of the cyclorotor (Leger, Pascoa, & Xisto, 2015).

Another advantage of the cyclorotor is its unique thrust vectoring capability that is achieved by varying the phase of the cyclic pitching. By thrust vectoring instead of pitching the vehicle forward, the cyclocopter can achieve level forward flight in a power-efficient manner. Previous wind tunnel studies on an isolated cyclorotor found that thrust vectoring enables a cyclocopter to potentially reach up to 13 m/s (29 mph) without relying on additional lift augmenting devices/surfaces. It was observed that the power required for a cyclorotor to maintain a steady, level flight significantly drops with forward speed, up to almost an advance ratio of 1.0, due to increased lift producing efficiency of the cyclorotor (Jarugumilli, Chopra, & Benedict, 2011). Thrust vectoring also improves maneuverability and capability of operation in gusty environments.

CHAPTER TWO

LITERATURE REVIEW

(Lee, Jung, & Hwang, 2004) carried out research on cycloidal blade system and cyclocopter in 2004, in which an analytical model was developed by using momentum theory and Blade element theory to examine the characteristic and performance of cyclocopter and to predict the thrust and power. Assuming the cycloidal blade system can be represented by a pair of actuator disks in tandem, the momentum theory and blade element theory was applied to the upstream half and downstream half of the rotor and induced velocity and thrust produced was calculated. The induced flow speed as a function of azimuth angle was observed in which the inflow speed was zero at azimuth angle 0° and 180° . Also, the flow speed increased with increased azimuth angle up to 90° and after this flow passed slowly. The flow pattern was symmetric about the vertical axis in the upstream but axisymmetric of the flow through the downstream rotor was lost because in the downstream total flow through the rotor flight path was composed of the component of the equilibrium of induced velocities. The induced flow in the region $180^\circ < \psi < 270^\circ$ in the downstream half of the rotor was entering the rotor while in $270^\circ < \psi < 360^\circ$ the flow was leaving the rotor. The magnitude of the flow velocity in the downstream rotor was smaller than that in the upstream. The lift coefficient variations with respect to blade azimuth angle was examined for a blade having chord to radius ratio $(c/R) = 0.375$ with camber effect or without camber effect. And it was found that the lift coefficient shifted downward by approximately 0.5 compared to that without camber effect. Whereas the vertical force component decreased in the upstream part but increased in the downstream part for a blade with camber effect. The aerodynamic forces and moment for the rotor span was calculated by integrating along the blade from the root to the tip. The total thrust produced on a rotor by all the blades was obtained by the resultant of all vertical forces and horizontal forces obtained from the resolution of the radial and tangential forces. Considering all profile drag and induced drag torque was calculated and thus the power required to turn the blades was obtained. The moving mesh method was used in CFD analysis to determine the aerodynamic design parameter and understand the flow conditions around rotor and blades. To improve the accuracy of CFD, Cycloidal Blade System (CBS) test apparatus

was generated, and results were compared. It was found that CFD analysis can predict the thrust of the CBS rotor as well. The experiments showed that the cycloidal rotor can produce thrust in any direction in the rotation plane and the rotor has hovering capability as well as forward flight capability.

From the experiment done after the development of the cycloidal blade system by implementing a sinusoidal low pitch system to investigate the fundamental characteristics in hovering state it was found that, with increase in rotating speed, pitch angle, rotor radius and number of blades, the thrust also increased. Whereas the efficiency decreased with increased number of blades as profile drag also increased and efficiency increased with increased rotor radius as it resulted in decreased solidity. Power increased rapidly as the rotating speed was increased in proportion to the cube of the rotating speed. Maximum thrust was generated at a pitch angle of 30° due to power limitation. Compared with hovering efficiency of other aircrafts it was found that cyclocopter had hovering efficiency higher than other aircrafts. They concluded that maximum hovering performance could be obtained at low rotating speed resulting in better efficiency and at low thrust level.

They designed a cyclocopter of 43kg including 7kg payloads and rotor torque was compensated by locating the center of gravity 50cm below in vertical direction and the 34 cm after in the horizontal direction from the rotor axis. They concluded that the cycloidal blades system can be used as a powerful thrust system capable of easy thrust vectoring, and the efficiencies for the aircraft with cycloidal rotor may compare favorably with values for other vertical takeoff and landing aircraft.

In 2005, (YUN, PARK, HWANG, & KIM, 2005) studied the mathematical modeling of thrust control mechanism of VTOL UAV and cyclocopter. They used sinusoidal low pitch system in which the control forces can be divided into the control force for magnitude of thrust (component in the direction of line joining center of the rotor and point of eccentricity) and the control force for direction of thrust (component perpendicular to the direction of line joining center of the rotor and point of eccentricity). The control of thrust direction was done by rotating mechanism and was calculated by formulating a numerical modeling to calculate the control thrust. It was found that when a control rod was located at the upper side of the CBS rotor, the load

applied to the control rod was compressible. Reversely, when a control rod was located at the lower side of the CBS rotor, the control rod was under tension loading state. The applied control force at the eccentricity points in the longitudinal direction over the range of $0^\circ < \Psi < 90^\circ$. Maximum force occurred at about $\Psi = 0^\circ$ and $\Psi = 90^\circ$. They concluded that the control of magnitude and direction of thrust can be done by a control block motion in a translation manner and the servo motors and servo linkages system must be selected and designed to be operated under the action of control force and torque.

In 2013, (Benedict, Jarugumilli, & Chopra, Effect of Rotor Geometry and Blade Kinematics on Cycloidal Rotor Hover Performance, 2013) investigated the effects of rotor geometry and blade kinematics on performance of the cyclorotor in terms of both thrust and power loading (thrust/power). They built a test setup with a load cell to measure the thrust, torque, and rotational speed of the cyclorotor. The baseline rotor they tested had a rotor diameter of 6-inch, blade span of 6.25-inch and chord length of 1.33-inch. The airfoil used was the NACA0015 and a hall effect sensor was used to measure the rotational speed. They studied the virtual camber effect and found that asymmetric blade pitching, and the pitching axis location can affect the performance of a cyclorotor. They varied the different parameters and studied the effects of the parameters on the performance of the rotor which include the rotor radius, blade span, chord, and blade planform. Radii of the rotor tested include 2, 3, 4, and 5 inches. Blade spans varied as 3.75, 4.69, 6.25 and 9.38 inches. Blade chords varied as 0.665, 0.887, 1.33, 1.665, 2 and 2.5 inch. The blade pitching amplitude of the rotor investigated includes 25° , 35° , 40° , and 45° with the rotational speeds ranging from 400 to 1800 RPM. On experimenting they observed that thrust and power does not vary much with radius, however thrust increased with increasing chord for constant blade speed. They concluded the power loading of the cyclorotor would vary significantly with radius for a constant chord. In contrast, their experiment showed that the power loading to disk loading was higher for a smaller rotor radius (2 inch for this case) keeping the chord constant. The experiment also concluded that power loading is identical if the chord/radius ratios are same even if the radii of the rotors are different. The chord/radius ratio of 0.835 yielded the best power loading with pitching angles of 40° and 1800 RPM. Power loading decreased drastically for chord/radius ratio more than 0.83. They

also concluded that the optimum chord/radius ratio is 0.8 and 0.5 for 40° and 20° pitching amplitude respectively.

Experiments carried with different blade spans with rotor radius 3 inch and chord 1.33 inch showed that thrust producing capability decreases linearly with blade span at constant speed. The article also states that the rotors with shorter span performed slightly better at higher disk loading for 40° pitching amplitude, the reason being not understood at that point. Another key conclusion made was, for a constant disk loading, the maximum power loading not only depends on the optimum chord/radius ratio but also on the total blade area of the rotor.

From the experiment carried out on the solidity, Benedict and associate researchers suggested that if solidity of the cyclorotor needs to be increased, the better approach is to increase the blade chord rather than increasing the number of blades using a smaller blade chord.

Benedict and his associates experimented on symmetric and asymmetric pitching either. For the symmetric pitching test, they used a 3-inch radius rotor, blades with 2-inch chord and 6.25-inch span as this was the optimum geometry obtained from their former experiments. They observed that increasing thrust by increasing the blade section angle of attack seemed more efficient than increasing the rotation speed. They concluded that maximum thrust which can be obtained by using this approach would still be limited by the onset of blade stall, and hence will be airfoil dependent since at low Reynolds numbers the profile drag coefficient is sensitive to the blade section angle of attack even before stall. For asymmetric pitching, the best power loading was obtained when the blades operated at a higher pitch angle at the top and a lower pitch angle at the bottom and the optimum blade kinematics was provided by pitch amplitude of 45° at top and 25° at bottom.

(Hrishikeshavan, Benedict, & Chopra, 2014) in 2014 in continuation to their research and experiment on the cyclorotor, performed another research and experiment on identification of flight dynamics of cyclocopter MAV in hover. For this purpose, they built an optimal performance cyclorotor with blade area/rotor area ratio of 0.35 and blade chord/radius ratio of 0.625. The maximum blade pitch angle of 45° was used and the airfoil used was NACA0015. They tested the flight dynamics where they

implemented the feedback control system to control the roll, yaw, and pitch of the cyclocopter. Their cyclocopter was controlled by an on board MSP430 microprocessor which worked in coordination with ITG3200 triaxial gyros, KXSD9 triaxial accelerometer and 2.4 GHz ATMEL transceiver. The attitude of the cyclocopter was as; pitch was controlled by controlling the speed of tail rotor, roll and yaw was controlled by controlling or providing differential speed to the cyclorotor. An important observation was that the roll and yaw degrees of freedom were tightly coupled due to gyroscopic effects.

As their primary objective they worked on the flight dynamics identification and analysis of maneuverability and gust disturbance rejection potential of a vertical takeoff and landing capable cycloidal rotor MAV. They performed systematic input excitation tests along all degrees of freedom in the closed-loop condition in hover, extracted the flight dynamics model using time-domain system identification techniques based on input and output data. It was found that the longitudinal and heave degrees of freedom were decoupled from the rest of the dynamics, whereas the lateral and yaw modes were highly coupled due to the gyroscopic effect.

(Hrishikeshavan, Benedict, & Chopra, 2014) continues their research focusing on developing control strategies for twin cyclocopter in forward flight and conducting wind tunnel testing. Here 550-gram vehicle was used with lateral dimension of 0.381 m, longitudinal dimension of 0.457 m and height 0.305 m with every cyclorotor having diameter of 0.152 m, blade span of 0.171 m, chord length of 0.051 m being driven by 75 Watts motor. Each blade uses NACA0015 airfoil. The chord to radius ratio was 0.625. A closed loop feedback control system was used for stabilizing along with a proportional derivative controller. Gyroscopic and control cross coupling is present which increases mainly at higher phase angles due to the increase in magnitude of propulsive forces there. So thrust vectoring has a larger impact on roll (left or right) moments and change in rotor rotation has a large impact on yaw moment (clockwise or counterclockwise). A positive roll(right) for the cyclorotor results in rotating speeds of the left motor to increase and right motor to decrease. At higher phase angles this gives a positive yaw(clockwise). So, this paper suggests that to get a pure roll controller should give command for positive roll with negative yaw(counterclockwise) which cancels yaw and negates effects of revolution per minute on yaw and results in pure roll

output. Similarly positive yaw with negative roll is needed to accomplish pure yaw output as well. Tests also conclude that for constant phase angle varying forward velocity does not significantly increase the coupling. According to the test the vehicle successfully demonstrated steady level forward flight up to maximum of 5m/s forward velocity and a satisfactory steady level forward flight was obtained with pitch and roll angles held close to zero. The rate of transition from hover condition to forward flight depends entirely on phase angle input. This paper also proves that when transitioning from forward flight to hover, a cyclocopter can immediately stop even when moving at an appreciable speed. At constant phase angle and forward velocity, increasing rotational speed resulted in an increase of both lift and thrust consequently increasing the power. However, increasing phase angle of the cyclorotor while keeping both forward velocity and rotational speed constant resulted in increase in thrust and decreased lift. Due to this this paper concludes that rotational speed and phase angle should be controlled for steady level flight (thrust = drag, lift = weight).

This paper (Leger, Pascoa, & Xisto, 2015) first proposes and then discusses an analytical or mathematical model to use during the design of cycloidal rotors. This uses semi-empirical ways to derive the relations. To prove the relations three different rotor configurations were used where rotor parameters like pitch amplitude, pitching axis location, blade chord, airfoil thickness and phase angle of eccentricity were varied. This model gave reliable estimation for thrust generated and power required operation of the cycloidal rotor when compared with experimental data from Bosch Aerospace, Seoul National university and IAT (Innovation Aeronautics Technologies) with deviation of data for forces of just 4.8%, 1.6% and 12.8% respectively and deviation for power of 4.2%, 8% and 3.4% respectively which shows this model is reliable. The relation was that thrust coefficient and power coefficient increase linearly with rotational velocity. During construction of the rotor, it is important to know about the motion of blades due to pitch mechanical control as it leads to non-perfect cycloid or to a pure cycloidal motion which is important to know for aircraft control. This paper also shows us that maximum pitch angle may be increased by increasing the magnitude of eccentricity. Maximum and minimum values of angular velocity and acceleration are affected by rotational speeds but the azimuthal angles where they occur are due to phase angle of

eccentricity phase angle. This model proposed by this paper is very important to define the control in lift and thrust forces when operating a cyclorotor based air vehicle.

In this article (Shrestha, Yeo, Benedict, & Chopra, 2017) designs a 60-gram cycloidal rotor for micro air vehicle tasks and analyzes which would be best design choices. To design data from previous studies are used here as well. Micro air vehicles are those aircraft with maximum dimension of 15 cm and maximum weight of 100 grams defined by Defense Advanced Research Projects Agency (DARPA) in 1997 (McMichael & S. Francis, 1997). The first objective here was to develop a lightweight cyclorotor. Most weight will be in the cyclorotor with each rotor having four composite blades. Here two cyclorotor with 60-gram weight are used. The cyclorotor uses NACA 0015 airfoil with maximum pitching amplitude of 45 degrees which are milled out of carbon fiber and evenly distributed along the span to maintain airfoil shape. This has minimum lateral dimensions of 0.178 m, longitudinal dimensions of 0.127 m and height of 0.153 m with diameter 0.076 m, blade span 0.043 m, chord of 0.022 m which are results from previous experiments. The pitching axis here has a carbon fiber spar that is present throughout the entire blade structure along with carbon fiber spar to provide a connection to the blade pitching mechanism. Here foam leading edge and stringers are used. This has managed to reduce the weight of the blade by 67% in comparison to conventional design. Four 0.5-gram blades on a twin cyclocopter are the preferred choice in this experiment. The chord to radius ratio is 0.57 and pitching axis location is 25% of blade chord. Tail rotor with 33 grams of thrust at 8000 rpm, closed loop feedback system with proportional derivative controller for stabilization are other features here. A horizontal tail rotor is used to counter the pitch down moment that occurs due to both rotors rotating clockwise. This capacity of the tail is increased by increasing the horizontal offset between this rotor and the vehicle's center of gravity according to this paper. The pitch down moment also causes unbalanced angular momentum and gyroscopic effect happens. Due to this, for a positive roll vehicle responds in both rolls right and counterclockwise and for positive yaw (clockwise) cyclocopter responds in clockwise yaw and rolls to the right. This is countered by mixing roll and yaw inputs of opposite types in the controller. This optimized cyclorotor has thrust to weight ratio of 3:1 at operational speed of 3000 rpm.

(HU, FU, ZHANG, WANG, & FARHAT, 2019) article shows the effects of the aspect ratio and taper ratio on the cycloidal rotor working at large pitching amplitude using the Unsteady Reynolds Averaged Navier–Stokes equations (URANS) solver. According to this paper hover efficiency is measured by figure of merit (FM) which is the ratio of ideal power to actual power and FM increases slightly with the taper ratio. However, it was found that improvement of FM is more significant due to airfoil and chord length than due to larger aspect ratio. The blades with the taper ratio equal to unity are the most efficient ones. This is due to the FM increases with the blade chord length when chord/radius ratio (C/R) is smaller than 0.5 and larger the taper ratio closer it approaches to 0.5. The aerodynamics force coefficients do not vary much with the aspect ratio. The greater the aspect ratio the more intense and concentrated downwash in the rotor cage. The efficiency slightly increases with aspect ratio but compared with the blade airfoil and chord length efficiency does not vary significantly with respect to aspect ratio. All the simulations were done using ANSYS Fluent and solvers used were: Incompressible Navier Stokes Equation and Pressure Implicit with Splitting of Operators. By the observation done by all the simulations and experiments they concluded that the hover efficiency is more dependent on the unsteady aerodynamic effects due to the blade pitching motion rather than the blade platform shape and should pay more attention to the blade airfoil and pitching motion, rather than the blade platform shape.

This journal (Gagno, Morandini, & Fournier, 2021) focuses mainly on efficiency optimization. It is known that cycloidal rotor efficiency is highly dependent on rotor diameter, angular velocity, and other geometric parameters. The important parameter to consider is weight which directly influences effective energy efficiency. Weight is interrelated with rotor dimensions and angular velocity, which changes the required structural strength.

The study reports optimal power loadings for: high chord/radius ratio; short spans; and solidity $\sigma \approx 0.4$. This article rather finds very low chord/radius and very low solidity. These discrepancies mostly highlight the different objectives of the two studies and the impact that the weight and material choice have on payload efficiency. As such, a simpler analysis could calculate the aircraft mass m_t by extrapolation.

A minimization technique with one objective function, 7 constraints, and 10 variables was used to yield an optimal configuration. The resulting configuration was presented in all its detail and the procedure used can be adapted to different cyclogyro designs. The whole procedure was carried out using open-source software, mainly the Sage Math and Dakota toolboxes. The method can also be modified to perform similar preliminary analyses for other 3D printed aircraft designs that require the optimization of efficiency. The method easily extends to studying supplementary parameters and configurations in order to obtain the best compromise between aircraft size, cost, flight time, flight velocity, efficiency, and payload.

This paper (Cogan & Gagnon, 2022) focuses on creating a model to give a good overview of the performance of a cyclorotor, trading accuracy for computational speed. cyclorotor with almost any combination of radius, blade number, profile, rpm, chord length, and pivot function. The model is tested with six blades, each using a NACA 0012 airfoil. A symmetrical airfoil is chosen because it must provide lift with both a positive and negative angle of attack.

Experimental thrust and power consumption values for varying cyclorotor configurations were gathered by the Korea Aerospace Research Institute. To measure only the aerodynamic effects of the blades, the weight of the scale and structure was subtracted from the thrust, and the power draw of the cyclorotor without the rotor blades was subtracted from the gross power draw. Both the maximum pitch angle as well as the rotational velocity are tested over a wide envelope to obtain a wide variety of results.

The results were obtained from 2D simulation and experimental model. Both were tested on different configurations varying rotational velocity and pitch. As the critical angle of attack is reached, the thrust produced dropped initially as flow separation occurred. However, as the angle of attack increased further, the lift began to increase again.

Comparing the thrust and power draw of several different CFD configurations, the thrust is as expected higher than the experimental values. With fewer disturbances and flow disruptions, the cyclorotor can displace more air in two dimensions than with a finite wing.

CHAPTER THREE

METHODOLOGY

3.1 REVIEW OF LITERATURES

Literature available on the development of cyclorotor, performance of cyclorotor, control characteristics of cyclorotor and cyclorotor pitching mechanism were reviewed for the knowledge of design parameter selection, part design realization, pitching mechanism realization and assembly techniques. Literature also served for simulation with the solvers dedicated for simulating cyclorotor aerodynamic characteristics. Most importantly the design parameters for the most optimized cyclorotor were obtained from the literature.

3.2 OBSERVATION

Results and reviews of different experimentalists' videos on the internet were observed which offered knowledge on the working of cyclorotor, parts design and assembly techniques, performance of different cyclorotor models and so on. Online videos for cyclorotor pitching mechanisms were observed multiple times for better understanding of the system for implementation on this project.

3.3 SOFTWARES EMPLOYED

3.3.1 CATIA V5

Catia V5 is a CAD software offering different workbenches for mechanical design and simulation. We used the software for 3D modeling the parts of our cyclorotor and simulation of the pitching mechanism. Part design workbench was used to model the parts of the cyclorotor. Assembly workbench was used for assembling the parts and components. Similarly, Digital Mockup (DMU) workbench was used to simulate the pitching mechanism of the cyclorotor. The Generative Shape Design workbench offered a platform for plotting the airfoil. Drafting workbench provided the platform for 2D realization of the solid parts.

3.3.2 XFLR5

XFLR5 is an analysis software for analyzing airfoils and wings. The software offers different features for modeling and analyzing the aerodynamic parameters of the airfoil. We utilized the Direct Foil Design workbench for plotting the airfoil and Xfoil Direct Analysis workbench for analyzing the lift parameters and other aerodynamic parameters of the airfoil.

3.3.3 OpenFOAM

OpenFOAM is a framework for developing application executables that use packaged functionality contained within a collection of over 100 C++ libraries. OpenFOAM is shipped with approximately 200 pre-built applications that fall into two categories: solvers, that are each designed to solve a specific problem in fluid (or continuum) mechanics; and utilities, that are designed to perform tasks that involve data manipulation. The solvers in OpenFOAM cover a wide range of problems in fluid dynamics.

OpenFOAM is supplied with pre- and post-processing environments. The interface to the pre- and post-processing are themselves OpenFOAM utilities, thereby ensuring consistent data handling across all environments.

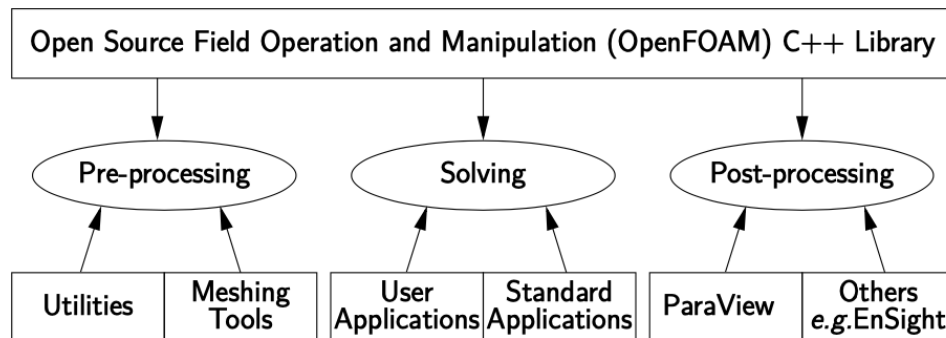


Figure 4 Overview of OpenFOAM structures

OpenFOAM is distributed with a large set of precompiled applications, but users also have the freedom to create their own or modify existing ones. Applications are split into two main categories:

Solvers are each designed to solve a specific problem in computational continuum mechanics.

Utilities that perform simple pre-and post-processing tasks, mainly involving data manipulation and algebraic calculations.

OpenFOAM is divided into a set of precompiled libraries that are dynamically linked during compilation of the solvers and utilities. Libraries such as those for physical models are supplied as source code so that users may conveniently add their own models to the libraries. This chapter gives an overview of solvers, utilities and libraries, their creation, modification, compilation, and execution.

3.4 PROJECT FLOW CHART

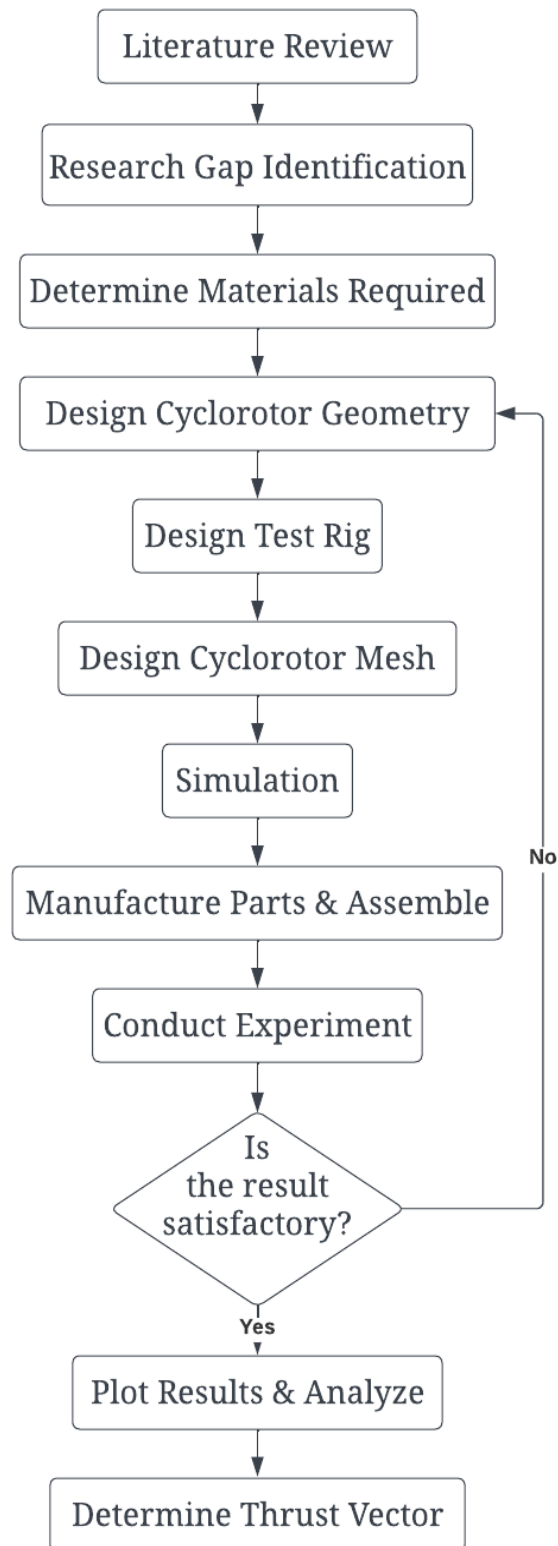


Figure 5 Project flow chart

CHAPTER FOUR

MATHEMATICAL MODELING

4.1 AIRFOIL MODELING

An airfoil is a shape of cross-section of wing, turbine and propellers which is designed such that it can produce desired lift, drag and aerodynamic properties when moved through a fluid medium such as air or water. Airfoil, although, is a closed shape contour; its shape can be discretized as shown in the figure below.

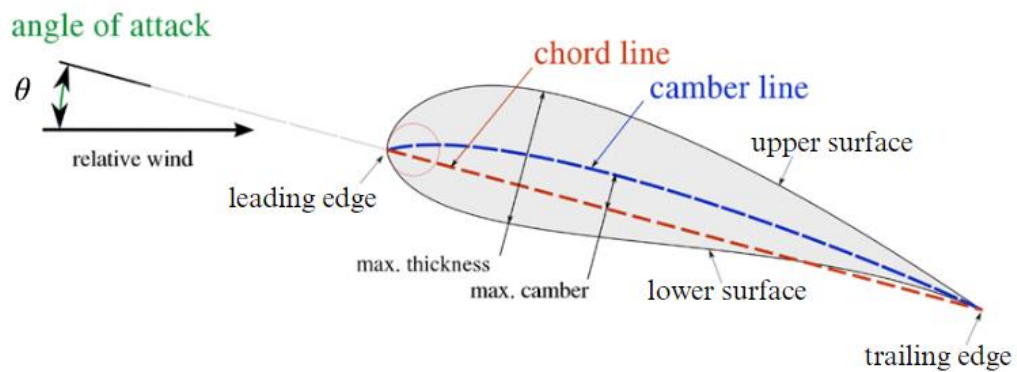


Figure 6 Airfoil nomenclature (*Source:*
https://en.wikipedia.org/wiki/File:Wing_profile_nomenclature.svg)

Airfoil can be classified on the basis of the camber it poses viz; symmetrical and cambered airfoil. Symmetrical airfoils have upper camber surface and lower camber surface mirrored about the chord line. The chord line and the camber line coincide in symmetrical airfoil. Whereas, cambered airfoils tend to have asymmetrical curves on the upper and lower surfaces. The camber can be positive and negative on the basis of the curvature orientation of the camber surface.

The coefficient of lift and coefficient of drag for an airfoil is dependent on the angle of attack (θ) which is the angle between the airfoil chord line and the free stream velocity.

$$c_l = c_n \cos\theta - c_a \sin\theta$$

$$c_d = c_n \sin\theta + c_a \cos\theta$$

where c_n and c_a are the normal force coefficient and axial force coefficient.

Also, the dimensionless aerodynamic parameters can be expressed in terms of dynamic pressure as follows:

$$c_l = \frac{L'}{q_\infty c} \quad c_d = \frac{D'}{q_\infty c} \quad c_m = \frac{M'}{q_\infty c^2}$$

where c_m is coefficient of moment

q_∞ is dynamic pressure.

Center of pressure is another important aerodynamic parameter which defines the stability of the wing body. It is that point on the body about which the aerodynamic moment is zero.

Mathematically,

$$x_{cp} = -\frac{M'_{LE}}{L'}$$

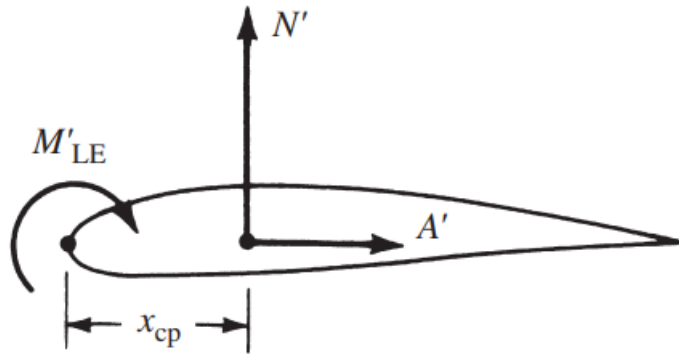


Figure 7 Center of pressure for an airfoil (Source: *Fundamental of Aerodynamics*, John.D.Anderson)

When the airfoil displaces fluid existing in its motion path, it produces aerodynamic forces namely, lift and drag which are functions of different aerodynamics properties.

Mathematically,

$$\text{Lift Force} \quad L = \frac{1}{2} \rho_{\infty} V_{\infty}^2 S C_L$$

$$\text{Drag Force} \quad D = \frac{1}{2} \rho_{\infty} V_{\infty}^2 S C_D$$

4.2 CYCLOROTOR

Mathematical modeling of a cyclorotor involves the use of equations that describe the aerodynamic forces acting on the blades, as well as the motion of the fluid around the blades. One common approach is to use the Navier-Stokes equations, which describe the motion of a fluid in terms of its velocity, pressure, and density, and to solve these equations numerically using computational fluid dynamics (CFD) software.

Mathematical modeling is an important tool for understanding the performance and behavior of cyclorotor and can help to optimize their design and operation for maximum efficiency and power output.

Using a new semi-empirical model, the thrust generated, and power required by the cycloidal rotor can be predicted (Leger, Pascoa, & Xisto, 2015). This is the important part of the design as it helps to analyze different parameters like:

1. Size of blade chord relative to the cyclorotor's radius
2. To describe eccentricity point
3. Positioning of the pivot point and distance between connection point of control rod and pivot point
4. Position of blades according to eccentricity phase angle
5. Distance between the blades

4.2.1 KINEMATIC MODEL

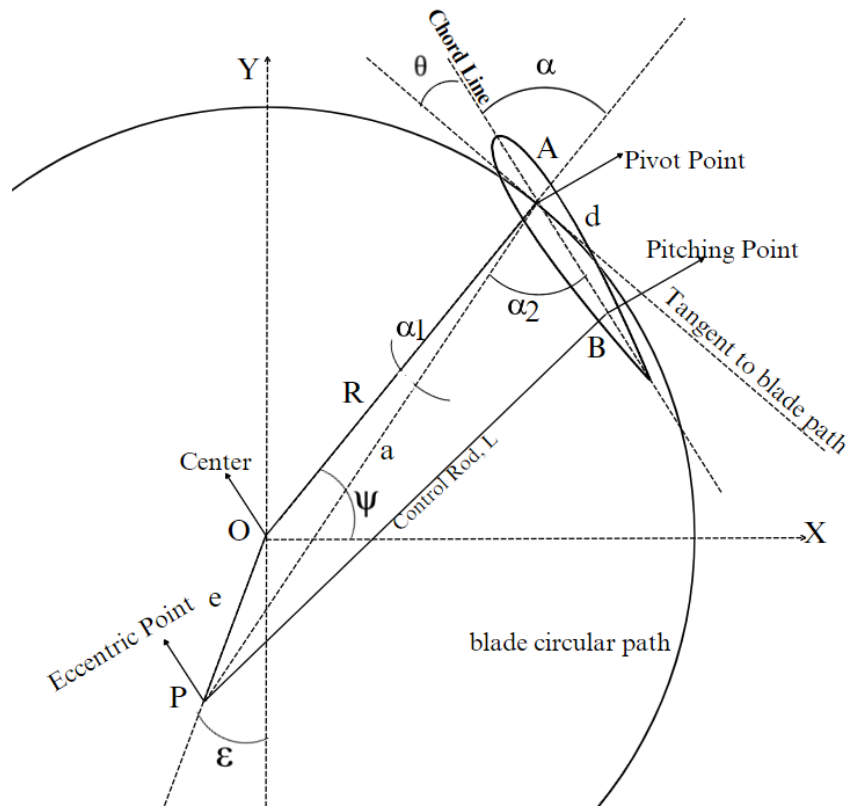


Figure 8 Blade control mechanism schematic

Here

$\Psi =$ azimuth angle

$\theta =$ Angle of attack

$e =$ eccentricity distance

$\varepsilon =$ eccentricity phase angle (phase angle)

$d =$ distance between pivot point and pitching point

$l =$ distance between eccentric point and pitching point

$R =$ distance between center and pivot point

$a =$ distance between eccentric point and pivot point

From *figure 8*

$$\theta = \frac{\Pi}{2} - \alpha$$

$$\alpha = \alpha_1 + \alpha_2$$

In ΔOAP

$$\frac{\sin(\alpha_1)}{e} = \frac{\sin(\frac{\Pi}{2} + \varepsilon + \psi)}{a}$$

In ΔPAB

$$\cos(\alpha_2) = \frac{a^2 + d^2 - l^2}{2ad}$$

Therefore

$$\theta = \frac{\Pi}{2} - \sin^{-1}\left[\frac{e}{a} \cos(\psi + \varepsilon)\right] - \cos^{-1}\left[\frac{a^2 + d^2 - l^2}{2ad}\right]$$

In general azimuth angle for different blades can be obtained by

$$\psi_i(0) = \psi_1(0) + \frac{(i-1)2\pi}{N}$$

Where $\psi_1(0)$ is one blade initial location and N is the number of blades.

The leading edge and trailing edge coordinates are given by (Leger, Pascoa, & Xisto, 2015):

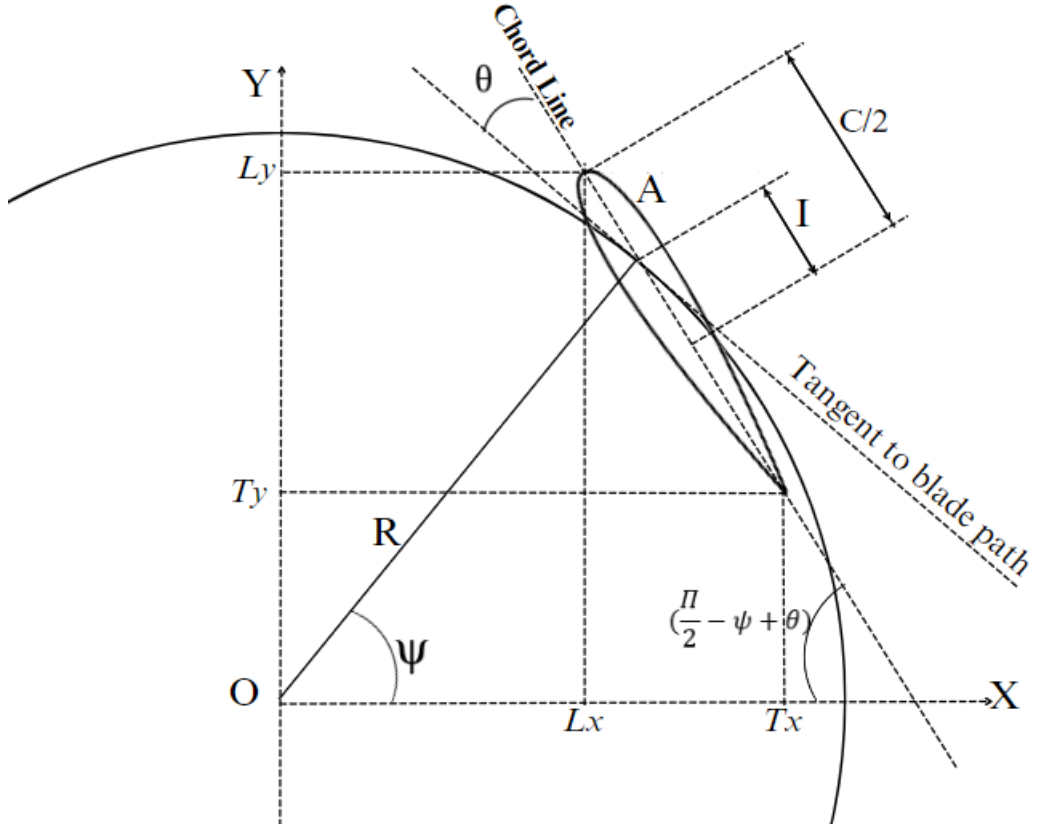


Figure 9 Leading and trailing edge coordinates

From *figure 9*

$$L_x = R \cos(\psi) - \left(\frac{c}{2} + I\right) \cos\left(\frac{\pi}{2} - \psi + \theta\right)$$

$$L_y = R \sin(\psi) + \left(\frac{c}{2} + I\right) \cos\left(\frac{\pi}{2} - \psi + \theta\right)$$

$$T_x = R \cos(\psi) + \left(\frac{c}{2} - I\right) \cos\left(\frac{\pi}{2} - \psi + \theta\right)$$

$$T_y = R \sin(\psi) - \left(\frac{c}{2} - I\right) \cos\left(\frac{\pi}{2} - \psi + \theta\right)$$

4.2.2 AERODYNAMIC ANALYSIS

Figure 10 represents the dynamic forces applied to the cyclorotor blade in hovering state. Here L is the lift, D is the drag, V_R is the resultant velocity associated with the induced downwash angle Φ .

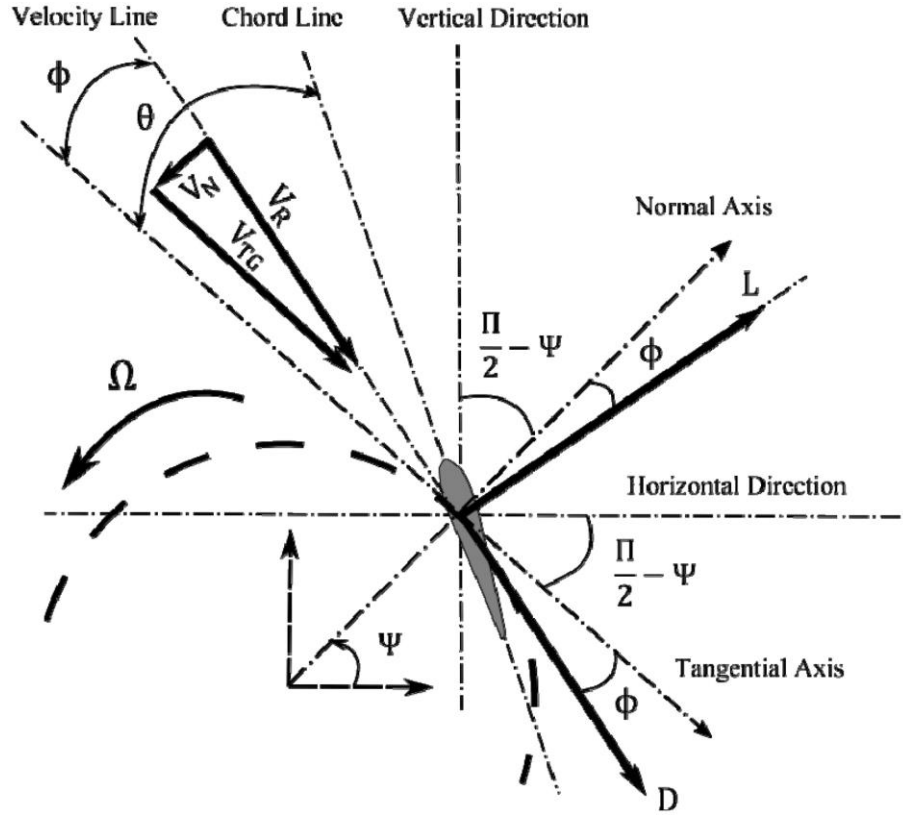


Figure 10 Horizontal and vertical resultant force components of blade in hovering state
(Leger, Pascoa, & Xisto, 2015)

The resultant forces in horizontal and vertical direction are given by:

$$F_x = L \cos(\psi - \phi) + D \sin(\psi - \phi)$$

$$F_y = L \sin(\psi - \phi) - D \cos(\psi - \phi)$$

The induced downwash angle is given by:

$$\phi = \tan^{-1} \frac{V_N}{V_{TG}}$$

The tangential component of resultant velocity is $V_R \cos \phi$ and the normal component is $V_R \sin \phi$.

The tangential velocity due to the rotor rotational movement is given by.

$$V_T = \Omega R$$

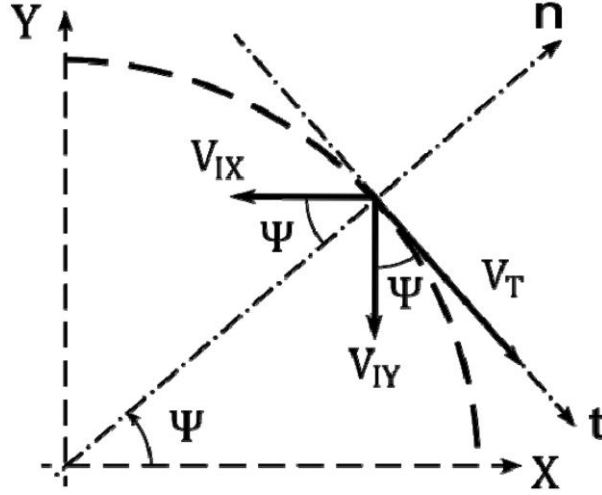


Figure 11 Analysis of induced velocities (Leger, Pascoa, & Xisto, 2015)

Figure 11 shows the induced down washed velocities depicted where V_{IX} is the induced velocity in horizontal direction and V_{IY} is the induced velocity in vertical direction.

The resultant velocity in tangential and normal direction are given by.

$$V_{TG} = V_T - V_{IX}\sin(\psi) + V_{IY}\cos(\psi)$$

$$V_N = -V_{IX}\cos(\psi) - V_{IY}\sin(\psi)$$

Now the induced velocities as the function of Φ can be expressed as

$$V_{IX} = V_T\sin(\psi) - V_R\sin(\psi + \phi)$$

$$V_{IY} = V_R\cos(\psi + \phi) - V_T\cos(\psi)$$

The 3-D lift curve of the cyclorotor airfoil is given by (McNabb, 2001)

$$C_{L\alpha 3D} = \frac{2\pi A_R}{2 + \sqrt{\left(\frac{A_R^2 4\pi^2}{C_{I\alpha}^2} + 4\right)}}$$

The two-dimensional unsteady lift is given by (Leger, Pascoa, & Xisto, 2015)

$$\frac{L}{S} = \rho b^2 (V_R \pi \omega - \pi b l acc) + C_{L\alpha 3D} \rho V_R b F [V_R (\theta + \phi) + b (\frac{1}{2} - I) \omega] \\ + \frac{C_{L\alpha 3D} \rho V_R b G}{\Omega} [V_R \omega + b (\frac{1}{2} - I) acc]$$

4.3 TRANSMISSION GEAR AND BELT

4.3.1 GT2 TIMING PULLEY

GT2 timing pulley is a toothed type of pulley used in power transmission systems in highly accurate positioning equipment. The teeth on the pulley provide proper engagement and prevent slippage during operations. “GT2” designation of this pulley refers to the type of the tooth profile used and stands for “Gates Tooth 2” in the honor of Gates Corporation who developed it.

The tooth profile features a trapezoidal shape with rounded root and a circular top providing higher torque transmission capacity, lower backlash, and reduced noise compared to other tooth profiles. GT2 timing pulley is designed specifically to work with GT2 timing belts.

The design of GT2 tooth profile involves different parameters and they are interdependent as well. Equations representing their relations can be shown as below:

1. Pitch Diameter (PD) - The diameter of the pulley where the belt makes contact.

$$PD = (N * TP) / \pi$$

where N is the number of teeth in the pulley.

2. Outside Diameter (OD) - The maximum diameter of the pulley.

$$OD = PD + 2 * TH$$

3. Root Diameter (RD) - The minimum diameter of the pulley where the belt enters the tooth groove.

$$RD = PD - 2.5 * TP$$

4. Tooth Height (TH) - The distance from the bottom of the tooth groove to the pitch diameter.

$$TH = BT * 2.17$$

5. Belt Thickness (BT) - The thickness of the belt.

$$BT = 0.64 * TP$$

6. Tooth Pitch (TP) - The distance from the center of one tooth to the center of the next tooth.

$$TP = 2 * T / (N + 2)$$

where T is the belt pitch

7. Tooth Profile Angle (TPA) - The angle between the tooth face and a line perpendicular to the pulley axis.

$$TPA = \text{atan}((TH - BT) / (\pi * PD / N - TP))$$

Since this tooth profile is designated as GT2 there are constraints to some parameters of the tooth such as.

- Tooth Height
- Tooth Pitch (which is 2mm since it is GT2)

4.3.2 GT2 TIMING BELT

GT2 timing belt refers to tooth type belt which has GT2 type tooth profile, specifically designed to work with GT2 timing pulley. The design parameters involved are same as that of the GT2 timing pulley, however the belt width and the belt length are the main constraints that are required to be carefully chosen. Guiding parameters for the selection of the belt are pitch of the belt (2mm for GT2 specifically), center-center distance between two pulleys, number of teeth on driver and driven pulley and torque to be transferred.

The belt length is a crucial parameter in belt selection and is dependent on the above-mentioned parameters. The belt length of a GT2 timing belt can be calculated using the following relation:

$$L = 2C + \frac{((N_2 + N_1) * P)}{2} + \frac{((N_2 - N_1)^2 * P^2)}{4\pi^2 C}$$

Where L is the belt length, C is the center-center distance between the two pulleys, N_1 and N_2 are the number of teeth on the driving and driven pulleys respectively and P is the pitch of the belt.

4.4 LOAD CELL

A load cell is a weight sensor which converts the force applied on it into an electrical signal measured in volts. The measured volt is then calibrated to the proper scale according to the sensitivity of the load cell and hence then used. The output voltage of a load cell can be calculated using the equation,

$$V_{out} = \left(\frac{F}{A}\right) * \left(\frac{E}{2}\right) * (L_2 - L_1)$$

Where F is force applied, A is the area of the load cell, E is the modulus of elasticity and L_2 and L_1 are the lengths of the load cell under load and without load, respectively.

Sensitivity is the ratio of change in output to the change in load applied to the load cell. This is the measure of the ability of the load cell to detect small changes in load applied. The sensitivity can be calculated using the expression,

$$S = (V_{outmax} - V_{outmin}) / F_{max}$$

Where V_{outmax} and V_{outmin} are the maximum and minimum output voltages respectively and F_{max} is the maximum rated capacity of the load cell.

CHAPTER FIVE

MATERIALS AND COMPONENTS SELECTION

5.1 MATERIALS FOR FABRICATION

5.1.1 PLA FILAMENT

PLA (Polylactic Acid) filament is a type of plastic that is commonly used in 3D printing. It is made from renewable resources, such as corn starch or sugarcane, and it is biodegradable, making it a more environmentally friendly option than some other types of 3D printing filament. PLA filament is known for its ease of use, as it is typically easier to print with than other materials, such as ABS (Acrylonitrile Butadiene Styrene). It has a lower melting temperature than ABS and is less prone to warping or shrinking as it cools, which makes it suitable for a wide range of 3D printing applications.

PLA filament is available in a range of colors and can be used to create a wide range of 3D printed objects, from prototypes and models to finished products. It is often used for educational or hobbyist projects, as well as for more professional applications. The mechanical properties of PLA filament depend on several factors, including the specific grade of PLA that is used, the processing conditions, and the environment in which the printed object is used. In general, PLA filament has the following mechanical properties:

1. *Tensile strength*: The tensile strength of PLA filament is typically in the range of 50-80 MPa (Megapascals). This is the maximum stress that the material can withstand while being stretched or pulled before it breaks.
2. *Tensile modulus*: The tensile modulus of PLA filament is typically in the range of 1200-3000 MPa. This is a measure of the stiffness of the material, and it indicates how much the material will deform under a given load.
3. *Impact strength*: The impact strength of PLA filament is typically in the range of 20-40 kJ/m². This is a measure of the material's ability to absorb energy when it is struck or impacted.

4. *Hardness:* The hardness of PLA filament is typically in the range of 80-90 Shore D. This is a measure of the material's resistance to indentation and scratching.



Figure 12 PLA filament spool

5.1.2 ALUMINUM TUBE

Aluminum is a lightweight and strong metal that is used in a wide range of applications, including the manufacture of tubes. The mechanical properties of aluminum tubes depend on several factors, including the specific alloy of aluminum that is used, the manufacturing process, and the condition of the material. The aluminum tubes available in the market are manufactured from different grades of aluminum (1000 – 7000 series). Here are some general mechanical properties of aluminum tubes:

1. *Tensile strength:* The tensile strength of aluminum tubes is typically in the range of 180-620 MPa (Megapascals). This is the maximum stress that the material can withstand while being stretched or pulled before it breaks.
2. *Yield strength:* The yield strength of aluminum tubes is typically in the range of 60-350 MPa. This is the stress at which the material begins to deform permanently.
3. *Modulus of elasticity:* The modulus of elasticity of aluminum tubes is typically in the range of 69-73 GPa (Gigapascals). This is a measure of the stiffness of the material, and it indicates how much the material will deform under a given load.
4. *Density:* The density of aluminum tubes is typically around 2.7 g/cm³. This is a measure of the mass of the material per unit volume.

5. *Thermal conductivity*: The thermal conductivity of aluminum tubes is typically around 205 W/m K. This is a measure of the material's ability to conduct heat.



Figure 13 Aluminum tube

5.1.3 CARBON FIBER ROD

Carbon fiber is a polymer that is a very strong lightweight material. They have several advantages including high stiffness, high tensile strength, low weight, high chemical resistance, high temperature tolerance and low thermal expansion. Carbon fiber is five-times stronger than steel and twice as stiff. Mechanical parameters of the carbon rod can be referred to from *appendix A table 6*.



Figure 14 Carbon fiber rod

5.2 COMPONENTS

5.2.1 GT2 TIMING BELT

The GT2 Belt is a timing belt built with Neoprene rubber with fiberglass core. It comes with an open loop or closed loop. The open loop belt is long and can be used by cutting it to our desired length however the closed loop has fixed length and number of teeth. The 'GT2' in its name refers to the specific tooth profile of the gear manufactured by Gates Corporation. The GT2 belt benefits in precision positioning, quieter operation, slip proof engagement, and higher power transmission efficiency.



Figure 15 GT2 timing belt

5.2.2 1400 KV BRUSHLESS DC (BLDC) MOTOR

A 1400KV brushless DC (BLDC) motor is a type of electrical machine that converts electrical energy into mechanical energy. It is called a brushless motor because it does not have brushes, which are used to transfer electrical current in traditional DC motors. Instead, brushless motors use electronic commutation, in which the phase of the electrical current is electronically controlled to produce rotational motion.

Brushless DC motors are known for their high efficiency, low maintenance, and good speed control. They are often used in applications where these characteristics are important, such as electric vehicles, robotics, and industrial automation. The 1400KV rating of the motor indicates that it can produce a high amount of torque for its size and weight, which can be useful in applications where a compact and powerful motor is

required. KV is a measure of the voltage that is required to produce one thousand RPM (revolutions per minute) of the motor's rotor.



Figure 16 1400 KV Brushless DC motor

5.2.3 ELECTRONIC SPEED CONTROLLER (ESC)

An Electronic Speed Controller (ESC) is an electronic circuit that is used to control the speed of an electric motor, such as the motor in a brushless DC motor. The ESC receives a signal from a controller, such as a radio transmitter or a microcontroller, and uses this signal to adjust the amount of power that is delivered to the motor. By controlling the power to the motor, the ESC can control the speed of the motor.

ESCs are commonly used in radio-controlled models, such as drones, planes, and cars, to control the speed of the motors that drive the model. They are also used in other applications where the speed of an electric motor needs to be controlled, such as robotics, electric vehicles, and industrial automation.

ESCs are usually designed to work with a specific type of motor, such as a brushless DC motor or a brushed DC motor. It is important to choose an ESC that is compatible with the motor that you are using, to ensure that the motor is supplied with the correct amount of power and that it operates safely. Since the power requirement for our model is very low being the test model small enough, we have selected 30 Amp ESC for this project which will serve our desired control of the motor.



Figure 17 30A Electronic Speed Controller

5.2.4 LITHIUM POLYMER BATTERY

A lithium polymer battery (also known as a Li-poly or LiPo battery) is a type of rechargeable battery that uses lithium-ion technology. It is called a "polymer" battery because the electrolyte that carries the lithium ions between the anode and cathode is suspended in a polymer matrix, rather than being a liquid as in traditional lithium-ion batteries. LiPo batteries are known for their high energy density, which means that they can store a lot of energy in a small space. This makes them a popular choice for portable electronic devices, such as smartphones, laptops, and tablets, as well as for radio-controlled models, such as drones and remote-controlled cars.

One of the main advantages of LiPo batteries is that they can be charged and discharged very quickly, making them ideal for applications that require rapid changes in power output. However, they can be more sensitive to abuse, such as overcharging or puncture, than other types of batteries, so it is important to use and handle them with care.



Figure 18 LiPo Battery 2200 mAh 3S

5.2.5 SERVO TESTER

A servo tester is a device that is used to test and calibrate servo motors. Servo motors are a type of electrical motor that is commonly used in radio-controlled models, such as drones and remote-controlled cars, as well as in robotics and industrial automation applications.

A servo tester typically consists of a power supply, a controller, and a display. It allows the user to send a signal to the servo motor and observe its response, such as its position or speed. This can be useful for diagnosing problems with the servo motor, adjusting its performance, or verifying that it is functioning correctly.

Servo tester can also be used to test a BLDC motor by connecting the servo tester with the ESC and powering the ESC with the battery. Here in this project, the servo tester serves both the function of actuating BL DC motor and a servo motor.



Figure 19 Servo tester

5.2.6 STEEL BOLTS AND NUTS

Steel bolts and nuts are fasteners that are used to hold two or more parts together. They consist of a bolt, which is a threaded rod with a head at one end, and a nut, which is a threaded cylinder that is tightened onto the bolt. Steel is a common material for bolts and nuts because it is strong, durable, and resistant to corrosion. There are many different grades of steel that are used for bolts and nuts, each of which has its own specific characteristics and properties. The most common grades of steel for bolts and nuts are grade 2, grade 5, and grade 8.

Grade 2 steel is a low-strength steel that is often used for light-duty applications. It is easy to work with and has good resistance to corrosion, but it is not as strong as higher-grade steels.

Grade 5 steel is a medium-strength steel that is often used for medium-duty applications. It is stronger and more durable than grade 2 steel, but it is still relatively easy to work with.

Grade 8 steel is a high-strength steel that is often used for heavy-duty applications. It is the strongest and most durable of the common steel grades, but it is also the most difficult to work with.

Bolts and nuts are available in a range of sizes and thread pitches to suit different applications. It is important to choose the correct size and grade of bolt and nut for the specific application to ensure that the fastener is strong enough to hold the parts together and that it is compatible with the other components in the system.

Highlighting the size of the test model and light application, grade 2 steel 3mm bolts and nuts have been used in this project along with compatible washers. Since the model is made of polymer and has much less strength compared to that of steel, we can assure the bolts and nuts will not fail during its operation.

5.2.7 STEEL MACHINE SCREWS

Steel machine screws are fasteners that are specifically designed for use with machine parts. They are made from a harder and more durable material, such as steel or stainless steel, and they have a more precise thread pitch than general screws. Steel machine screws are typically used with a tapped hole, which is a hole that has been threaded to match the thread pitch of the screw. This allows the screw to be tightened securely into the hole and ensures that it holds the parts together with a high level of precision.

The machine screw used in this project came along with the brushless motor which we procured. The screw is used to mount the motor to the motor mount and hence fixes the motor rigidly to the substrate.



Figure 20 Steel machine screw

5.2.8 LOAD CELL

A load cell, also known as a weight sensor or strain gauge, is a device that is designed to measure a specific force in one direction. It consists of a carefully designed metal structure with small elements called strain gauges mounted in precise locations on the structure. When a load is applied, the structure deforms and the strain gauges measure the deformation, which is then converted into an electrical signal that can be amplified and measured. Load cells are made of aluminum alloys and are sensitive to forces only along the vertical direction as prescribed by the manufacturer. They require a load cell amplifier such as the HX711 load cell amplifier or the 1046 PhidgetBridge for electrical signal output.

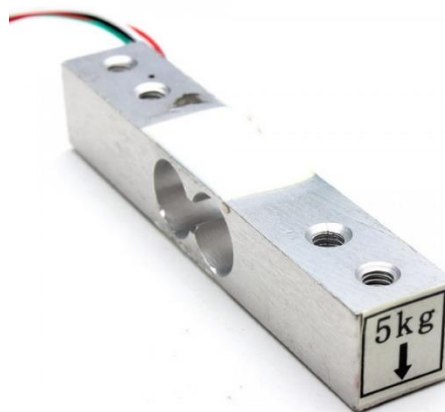


Figure 21 Load cell

5.2.9 HX711 MODULE

The HX711 module is an amplifier that provides an interface to communicate with the load cell. This module is named HX711 since it is engraved with the HX711 chip which has 24 high precision A/D converters. This includes an on-chip low-noise amplifier (LNA) that can amplify the small signals from the load cell or strain gauge to make them more easily measurable. The HX711 can operate from a single power supply and has two differential input channels that can be used to connect to the load cell or strain gauge. The module also includes a programmable gain amplifier (PGA) that allows the user to adjust the gain of the amplifier to match the specific needs of the application. The module can interface with a microcontroller using its library which is available open source. The HX711 library offers the interface for calibration as well as the read test facility which provides real time data acquisition.

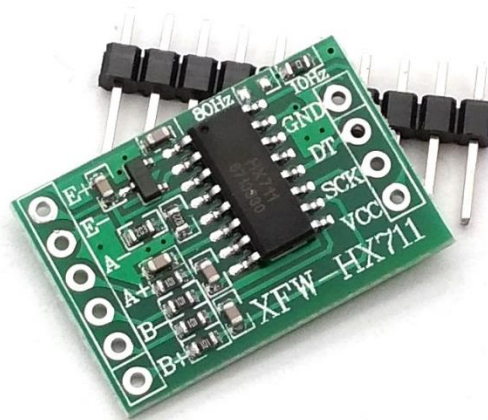


Figure 22 HX711 Amplifier

5.2.10 ARDUINO UNO

The Arduino Uno is a microcontroller board based on the ATmega328P. It has 14 digital input/output pins, 6 analog inputs, a 16 MHz quartz crystal, a USB connection, a power jack, an ICSP header, and a reset button. It is widely used in various DIY projects, robotics, and electronic devices. It can be programmed using the Arduino software, which is based on C/C++ programming languages. The board can be powered either through the USB connection or an external power supply. It has a built-in voltage

regulator that can regulate the input voltage between 7V to 12V. The board also has a wide range of shields, which can be used to extend its functionality.

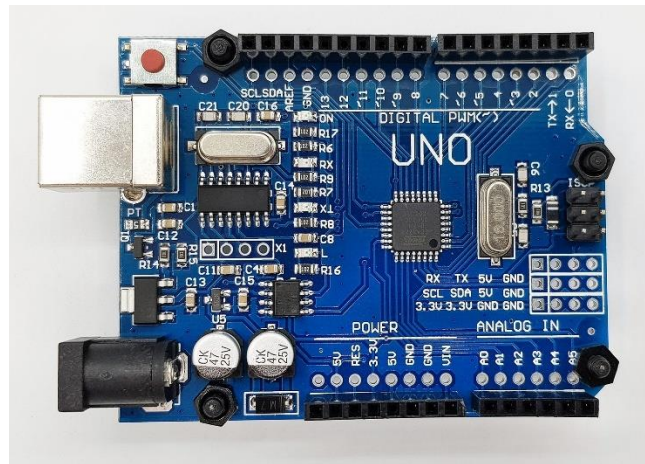


Figure 23 Arduino Uno

CHAPTER SIX

DESIGN, SIMULATION AND ANALYSIS

6.1 AIRFOIL DESIGN AND ANALYSIS

Airfoil design is very crucial on a project like this since the primary functioning part of the system to meet the objective is the airfoil blade. Airfoil is responsible for producing the desired lift when it is subjected to moving air. Although there are different parameters responsible for generation of lift, characteristics of lift generation are also important according to the system that the airfoil blade has been employed on. Our system has a feature such that one airfoil can contribute twice to lift generation in one revolution of the rotor allowing both the surfaces of the airfoil blade to contribute according to its position in the plane of rotation. Due to this unique feature of the cyclorotor the airfoil to be used in this system requires both the surfaces to produce equal and adequate lift during operation which is possible only with the symmetric airfoil. Hence symmetric airfoil has been used in this project.

Although the symmetric profile of the airfoil has been selected, specific type and design parameters of airfoil are difficult to state. For this reason, we have chosen NACA0015 airfoil with 2-inch chord since it has been found to be an optimal airfoil for the cyclorotor from previous experiments (Benedict, Jarugumilli, & Chopra, Effect of Rotor Geometry and Blade Kinematics on Cycloidal Rotor Hover Performance, 2013).

Analysis of NACA0015 airfoil using XFLR5 software with Reynolds number 39,941 (calculation shown in later section) and the angle of attack varying from -10° to 60° with increment of 0.3° gives the following polar curves. The curve shows that the value of coefficient of lift increases with increase in angle of attack. The value of coefficient decreases sharply after 9° . As the angle of attack increases further than 9° the coefficient of lift starts to increase again. This is called post-stall lift. Since for this experiment the maximum angle of attack that the cyclorotor blade will encounter is 40° hence the coefficient of lift corresponding to the 40° angle of attack obtained from the curve is 1.21.

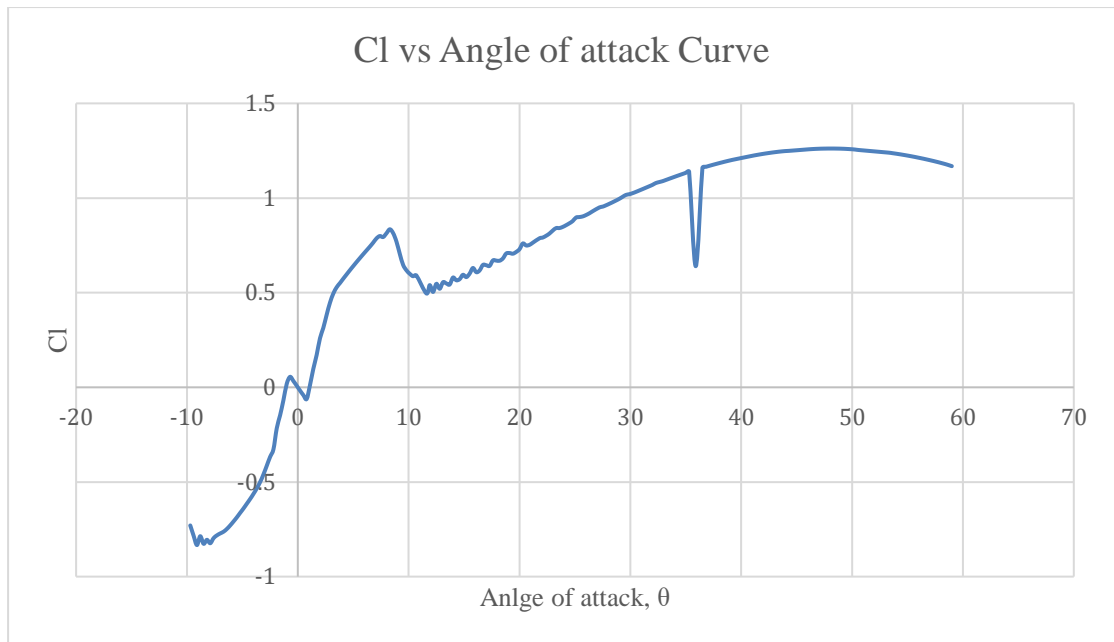


Figure 24 Coefficient of lift vs angle of attack curve

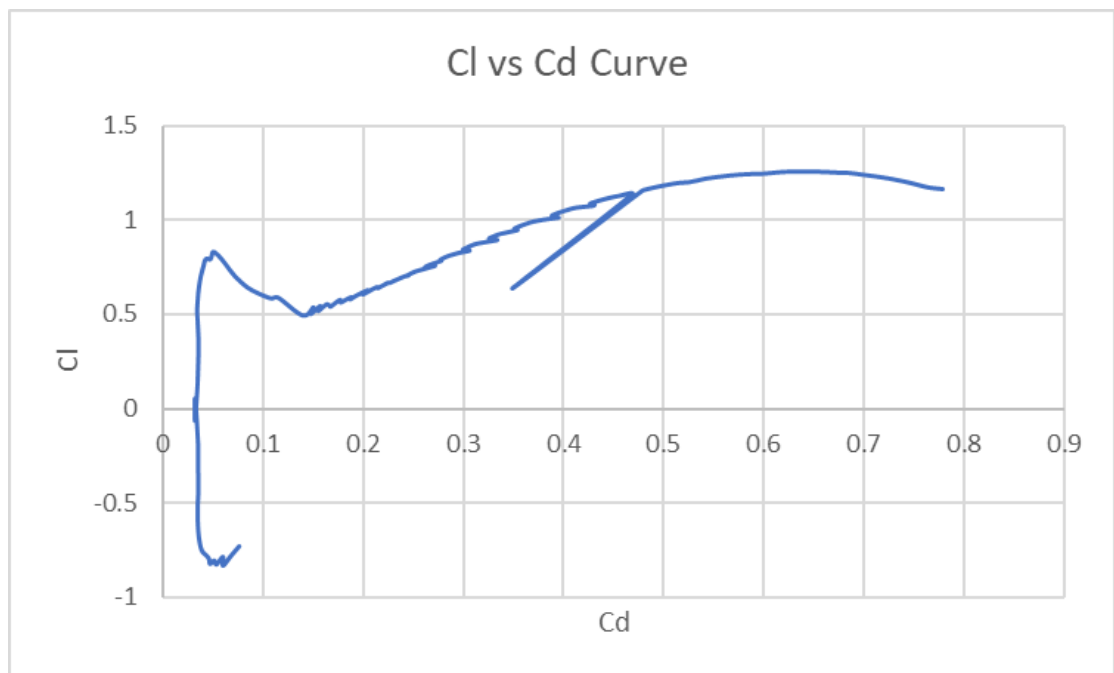


Figure 25 Coefficient of lift vs coefficient of drag curve

Numerical calculation for obtaining the maximum lift produced

$$\text{Chord length} = 50.8 \text{ mm}$$

$$\text{Density of air} = 1.225 \text{ kg/m}^{-3}$$

$$\text{Area} = 50.8 \times 10^{-3} \times 171 \times 10^{-3} = 8.686 \times 10^{-3} \text{ m}^2$$

$$\text{RPM} = 1400$$

$$\omega = 146.607 \text{ rad /s}$$

$$\text{velocity (v)} = 11.17 \text{ m/s}$$

$$\text{Kinematic viscosity (}\nu\text{)} = 1.42 \times 10^{-5}$$

$$\begin{aligned}\text{Reynolds number (}R_e\text{)} &= \frac{v \cdot l}{\nu} \\ &= \frac{11.17 \times 0.0508}{1.42 \times 10^{-5}} \\ &= 39,941\end{aligned}$$

$$\text{Maximum lift force} = 2 * \text{lift produced by each blade}$$

$$\begin{aligned}&= \rho * v^2 * A * C_l \\ &= 1.225 \times 11.17^2 \times 8.686 \times 10^{-3} * 1.21 \\ &= 1.6063 \text{ N} \\ &= 163.74 \text{ g}\end{aligned}$$

6.2 ROTOR DESIGN

Rotor design involves consideration of several factors to ensure proper function ability and efficient operation of the cyclorotor. A rotor is an assembly of mainly two parts: airfoil blade and rotor wheels. The main factor that is to be considered on the airfoil blade after aerodynamics is the strength of the airfoil blade so that it can bear the

bending stress and shear stress generated due to lift produced during the operation. Similarly, for the rotor wheel, tensile stress is a major consideration since the point of joints transfer tension produced by the virtue of lift generation by blade holder element. Efficient cyclorotor is the key requirement of this project as its object is to study the thrust vector curve generated due to the variation in eccentric phase angle.

6.2.1 ROTOR WHEEL

Much research had been done previously where the objective was to develop an efficient and optimized cyclorotor. Referring to those research and experiments, some design parameters for our experiment have been chosen based on optimized and efficient cyclorotor.

The radius of the rotor is chosen to be 3 inches which is claimed to be a proven optimal design parameter (Benedict, Chopra, & Gupta, Design, Development and Open-Loop Flight-Testig of a Twin-Rotot Cyclocopter, 2013). The 3-inch rotor radius gives the chord/radius ratio of 0.67 which is in the range of 0.5 and 0.8 and shows viability according to the statement presented in the previous literature. The maximum amplitude of pitching is chosen 40° as per the same literature since these constraints define the cyclorotor to be optimal.

Considering the carbon spar element to be undeform-able and rigid (to be discussed in subsequent sections) we design the rotor wheel impact site portions. The force applied to the site is by the carbon rod fitted inside the hole of the rotor wheel and is tensile or compressive according to its position in the plane. The lift generated is the amount of load applied to the sites hence, limiting our maximum lift attainable to 200 grams we calculate the tensile stress on the rotor wheel section.

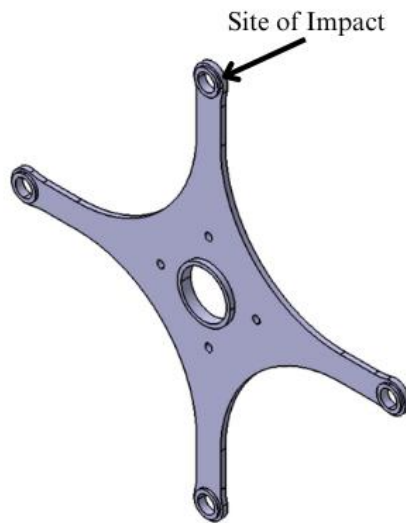


Figure 26 Rotor wheel tensile stress vulnerable site

Since two blades are responsible for lift generation at once, the contribution of each blade is equal. Hence the lift generated by each blade is 100 grams. Again, the blade is attached to the two rotor wheels on each end and lift force acts from the center of the blade, each rotor joint point will experience 50 grams of lift force. Hence taking the force of 50 grams as the load applied, we find the tensile stress on the section of the rotor.

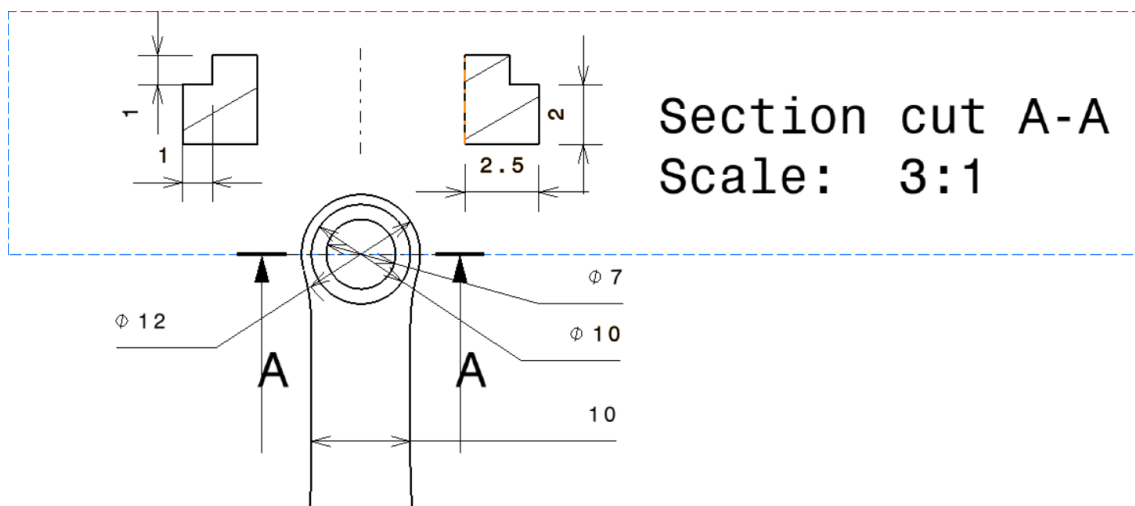


Figure 27 Section of the vulnerable impact site

Tensile Stress

$$\sigma = \frac{F}{A}$$

Where $F = 50 \text{ grams} = 0.4905 \text{ N}$

and $A = 2 * ((2.5 * 2) + (1.5 * 1)) = 13 \text{ mm}^2$

Hence, tensile stress

$$\sigma = 37,730.77 \text{ Pa}$$

The strength of the material used to manufacture the part is in the range of 50 – 80 MPa hence the part will not fail in tension during operation.

6.2.2 AIRFOIL BLADE

Aerodynamics regarding the airfoil has been discussed in the preceding section, thus this section will be oriented on the mechanical parameters of the airfoil blade i.e., the strength of the airfoil blade. Before proceeding with the mechanical strength of the blade, the blade dimension is paramount. From literature review it is found that the optimal configuration for a cyclorotor is the blade span equal to the rotor diameter (Kirsten, 1928). Again, the latest experiment from (Benedict, Chopra, & Gupta, Design, Development and Open-Loop Flight-Testig of a Twin-Rotot Cyclocopter, 2013) shows that the most optimal configuration of cyclorotor has a blade span of 6.25 inch. Hence referring to those results and statement the blade is set to 171 mm (~6.7 inch). The extra blade span resulted from the mount that is used to hold the blade hence giving an effective blade span as 6.25 in.

The blade is subjected to bending stress and shear stress due to the lift which is acted uniformly throughout the blade. The carbon rod is used as the reinforcing element and contributes for assembling the airfoil blade to the rotor wheel as well. From Figure 23 we can see that the blade loading is of simply supported beam type with uniformly distributed lift force acting throughout the length of the blade. Hence the bending stress and shear stress can be computed using the uniformly distributed lift force of 0.5848 gram/mm in each blade. The reinforcement is provided by two carbon fiber rods; hence the bending stress will be experienced by both the rod along with the surface of the blade.

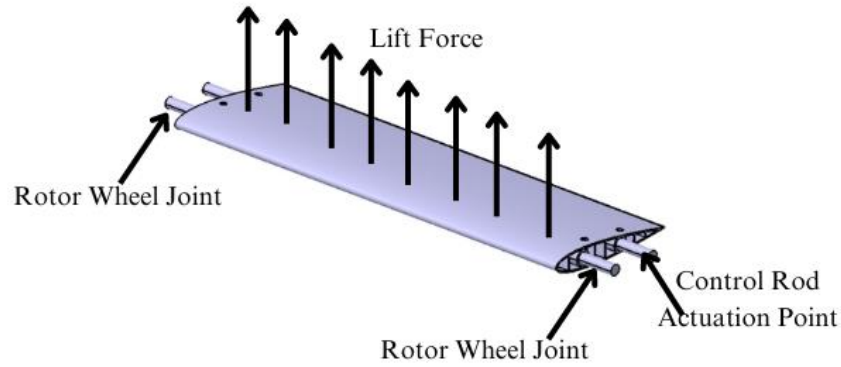


Figure 28 Blade force diagram

Shear stress can be calculated using the following relation.

$$\tau = \frac{4V}{3A}$$

Where $A = 12.5664 \text{ mm}^2$

$V = 50 \text{ gram}$ (from *appendix A figure 61*)

Hence the maximum shear stress that exists on the carbon rod is 52,043.6664 Pa.

Bending stress on the blade element is calculated as,

$$\sigma_m = \frac{Mc}{I}$$

Where $c = 2\text{mm}$

$I = 12.5664 \text{ mm}^4$

$M = 2137.5 \text{ gm mm}$ (from *appendix A figure 62*)

Hence the maximum bending stress persists at the center of the spar length and the magnitude of the stress is 3.3373 MPa.

From the appendices table 3 we can compare that the stresses generated are much lower than their limits hence the carbon fiber rod of 4 mm is viable for our use in the project.

If the optimal design is considered the diameter of the carbon rod can be much lesser as 1 mm, however, for ease of fabrication this dimension is restrained for this project.

The best location of the airfoil pitching axis is at 25 % of the chord from the leading edge of the airfoil (Shrestha, Yeo, Benedict, & Chopra, 2017). Considering all the factors that have been well studied and experimented with previously our design parameters were obtained as shown in the table below.

Table 1 Design parameters for the cyclorotor used in this project.

S.No	Parameter	Value
1	Rotor Diameter	152.4 mm
2	Total Blade Span	171 mm
3	Chord Length	50.8 mm
4	Pitching axis location	25% of chord from leading edge
5	Actuation point in airfoil	17.5 mm from Pitching axis
6	Total length of control rod	76.2 mm
7	Carbon Rod Spar	4 mm (diameter)

6.3 TRANSMISSION DESIGN

6.3.1 GEAR DESIGN

A GT2 timing pulley has been used in this project for transferring the power from motor to the cyclorotor. The selection of the gear pulley involves torque requirement and speed requirement. In this project the torque offered by the motor is adequate hence torque multiplication factor shall not be of paramount interest rather the speed is crucial since the RPM range is limited on the lower range for cyclorotor. Because our model has been experimented with 4800 RPM in recent experiments, we allocate the maximum RPM for our cyclorotor as 5000 RPM. The driver gear is chosen of 20 teeth since 5 mm bore diameter is the main constraint and with this requirement of bore size other lower size of the driver pulley is not possible and another bigger option is not chosen due to dimensional limitations. The driven gear has 60 teeth. This set of gear gives a torque multiplication factor 3, being the speed reduction factor 3. The calculation has been shown below:

Constraints

Motor specification:	1400 KV
Maximum obtainable RPM:	15540 RPM (with 3S battery)
Required range of RPM:	0 - 5000 RPM
Minimum size of GT2 timing pulley available:	20 Teeth / 5mm Bore (appendices figure)

Calculation for gear ratio

$$\begin{aligned}\text{Gear Ratio} &= \frac{\text{Max RPM available on the motor shaft}}{\text{Max RPM required on the cyclorotor shaft}} \\ &= \frac{15400}{5000} \\ &= 3.108\end{aligned}$$

Rounding off the value and taking the integer only, the gear ratio is 3.

Calculation for number of teeth required on driven GT2 timing pulley required.

$$\begin{aligned}\text{Number of teeth required} &= \text{Number of Teeth in Driver Gear} * \text{Gear Ratio} \\ &= 20 * 3 \\ &= 60 \text{ Teeth}\end{aligned}$$

6.3.2 BELT DESIGN

Belt design involves belt width and belt length determination along with the tooth profile. For the case of GT2 timing pulley, GT2 timing belt is specifically manufactured by the manufacturer. Hence the design parameters are the belt width and the belt length for this project. The pitch of the belt to be used is 2 mm since it is a GT2 timing belt, and the center-to-center distance is 58 mm set according to dimensional feasibility in the model. With the data provided the belt length is obtained to be 198.7951 mm and the belt length in catalog near to this value is 200 mm. Hence a 200 mm GT2 timing belt has been used.

For the width of the belt, *table 5* from *appendix A* is referred which shows that 1 mm width has 86 N breaking strength which is more than required but since 1 mm width belt is not available and the lowest size available is 6 mm, it is chosen for the cyclorotor driver system.

6.4 SIMULATION OF CYCLOROTOR

The CFD model is tridimensional and uses the finite volume method to solve the PIMPLE algorithm, which consists of a merger of the PISO and SIMPLE algorithms.

OpenFOAM is used for the simulation of the model.

6.4.1 SOLVERS

In this project pimpleFoam is used. pimpleFoam uses the PIMPLE algorithm. The PIMPLE algorithm combines the PISO (Pressure Implicit with splitting of operations) and SIMPLE (Semi-Implicit Method for Pressure Linked Equations) algorithm. This algorithm is an iterative procedure for coupling equations of momentum conservation and momentum conservation. The PIMPLE algorithm is mainly used for transient

problems. Within steps, in time this algorithm solves a pressure equation to enforce mass conservation, with an explicit correction to velocity to satisfy momentum conservation. The principle of this algorithm is as follows.

Within a single time-step, a steady-state solution is searched while an under-relaxation strategy is applied. After the solution is found, we go to the next time-step. For this, we need the so-called outer correction loops, to ensure that all explicit parts of the equations are converged. After a user-defined tolerance criterion is reached within the steady-state calculation the outer correction loop is left, and we move on in time. This is done until the simulation end time is reached (Greenshields C. J., 2018).

Outer correctors: The number of Outer correctors of the PIMPLE algorithm defines how many outer iterations to perform, that is, how many times the system of equations are performed before it is forced to move onto the next time step, regardless of whether that time step has converged or not. If the step convergence is reached before the number of iterations is reached, then it will stop and move on to the next time step. The (Greenshields C. , 2018) criteria for time step convergence are defined as the absolute tolerance of the solver (SimScale, 2020).

Inner correctors: The number of inner correctors is the number of times the pressure is corrected within an iteration. Typically, this should be set low. Many correctors rarely improve results and should conform to this recommendation.

The PIMPLE algorithm below is cited and explained as proposed by Holzmann (Holzmann, Mathematics, numerics, derivations and OpenFOAM®, 2019). The steps from 1 to 4 represent the first loop, while the correcting second loop begins on step 5, each one coupling pressure and momentum once.

Construct momentum matrix:

$$U_t + \nabla \cdot (UU) + \nabla \cdot R = -\nabla \cdot p$$

Construct the pressure matrix using the momentum matrix.

$$\nabla^2 p = f(U, \nabla p)$$

Calculate pressure.

$$p_{new}$$

Correct the velocities with the new corrected field.

$$p_{new} \rightarrow U_{corrected}$$

Reconstruct the momentum matrix with new velocities.

$$\frac{U}{\delta t} + \nabla \cdot (UU) + \nabla \cdot R = -\nabla p$$

Construct the pressure matrix using the momentum matrix with the new velocities.

$$\nabla^2 p = f(U, \nabla p)$$

Calculate pressure.

$$p_{new}$$

Correct the velocities with the new pressure field.

$$p_{new} \rightarrow U_{corrected}$$

6.4.2 TURBULENCE MODELING

Turbulent phenomena occur temporally, as well as spatially, fine scales, extreme computing resources would be required to investigate them using basic CFD methods. This is the case for 'Direct Numerical Simulations' (DNS), which are rarely practical, because they demand extremely fine grid spacings and time steps. To treat turbulent phenomena in a more efficient way, multiple, mostly empirical turbulence models have been designed by CFD engineers. The choice is the commonly used URANS-method (unsteady Reynolds averaged Navier-Stokes), which models turbulent variables like velocity u and pressure p using a statistically averaged (e.g., u) and a variable component (u'):

$$u = \bar{u} + u'$$

Applying the above equation to the Navier-Stokes-equations leads to the expression $u'v'$. These terms are difficult to close, which is why semi-empirical models are commonly used, adding up to 2 transport-equations. In the current work, k- ω -SST-Model is the method of choice.

6.4.3 THE SST K- ω TURBULENCE MODEL

The SST k- ω turbulence model is a two-equation eddy-viscosity model that is used for many aerodynamic applications. The k- ω model is the model of choice in the sublayer of the boundary layer. Unlike any other two-equation model, the k- ω model does not involve damping functions and allows Dirichlet boundary conditions to be specified. Because of its simplicity the k- ω model is superior to other models in case of numerical stability. It is also as accurate as other models in predicting flow profile.

6.4.4 ARBITRARY MESH INTERFACE (AMI)

To simulate rotating motion, *Arbitrary Mesh Interface* (AMI) is used in OpenFOAM. The inner zone rotates relative to the outer zone. The AMI interpolates inner and outer mesh to achieve a coupling of two meshes that are rotating relative to each other. In OpenFOAM *cyclic AMI boundary* conditions can be used to couple these zones. In our project a total of 5 moving mesh use sliding interfaces of interpolation. They are solved by the Arbitrary Mesh Interface (AMI) algorithm. Each rotor blade is inserted into a double AMI. The outer AMIs rotate, and the inner ones strongly oscillate. The inner cell zone includes the blade surfaces and are referred to as AMI-cylinders. To avoid sharp corners, which are generally detrimental to mesh quality, the AMI-cylinders have a hemispherical base area. (Donners, 2022)

6.4.5 MESHING

The background mesh between the cylinders and the far field is created using OpenFOAM's automatic meshing tool *snappyHexMesh*. *blockMesh* is used to create cartesian structured grid. The *snappyHexMesh* automatically refines specified areas, snap to surfaces and is also capable of adding boundary layers. The resulting grid is hexahedral unstructured.

The snappyHexMesh utility generates 3-dimensional meshes containing hexahedra (hex) and split-hexahedra (split-hex) automatically from triangulated surface geometries in Stereolithography (STL) format. It then refines the volume mesh near and on surfaces in portions of surfaces that are close to other surfaces and inside user-defined regions. Refinement is applied as a user-specified number of subdivisions to the original structured mesh. Cells are refined either inside or within a specified distance of a given region or when intersecting a given surface. Once the mesh is refined, the cell faces are moved to smoothly adhere to the boundaries, which can be wall boundaries or simple reference geometries. This last option allows us to create the sliding interfaces of the blade oscillating zones and the rotor spinning zones. The size of the (Holzmann, Mathematics, numerics, derivations and OpenFOAM®, 2019) mesh and the time it takes to generate are controlled by quality and iteration options (Holzmann, Mathematics, numerics, derivations and OpenFOAM®, 2019).

It is notable that the mesh only includes the airfoils as aerodynamic surfaces, but not the axle nor any rods. This is to keep the interfaces simple, as rods would require multiple surfaces that are in direct contact and nevertheless moving relative to each other. Furthermore, the aerodynamic influence of these surfaces is expected to be limited to moderate power losses, which is why this simplification is deemed permissible. (Donners, 2022)

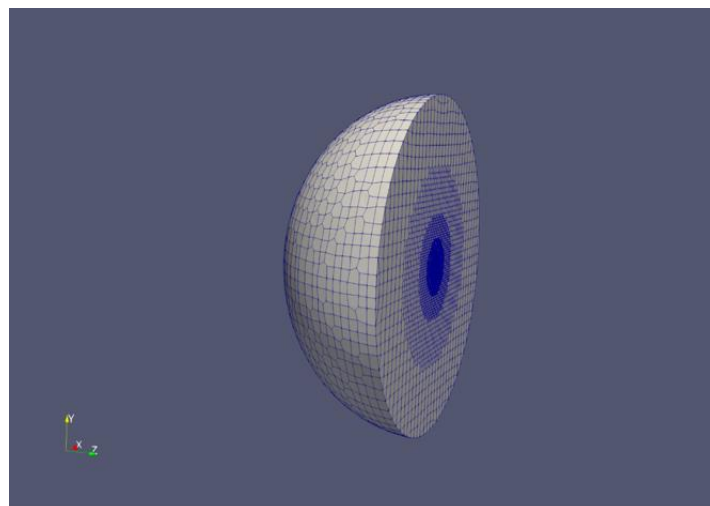


Figure 29 Refined mesh sphere

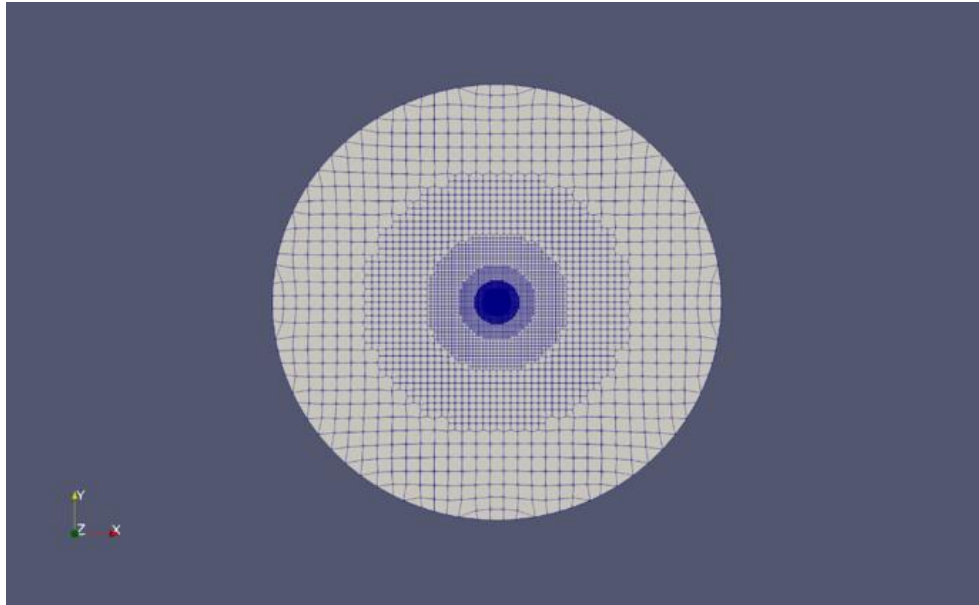


Figure 30 Front view of the mesh

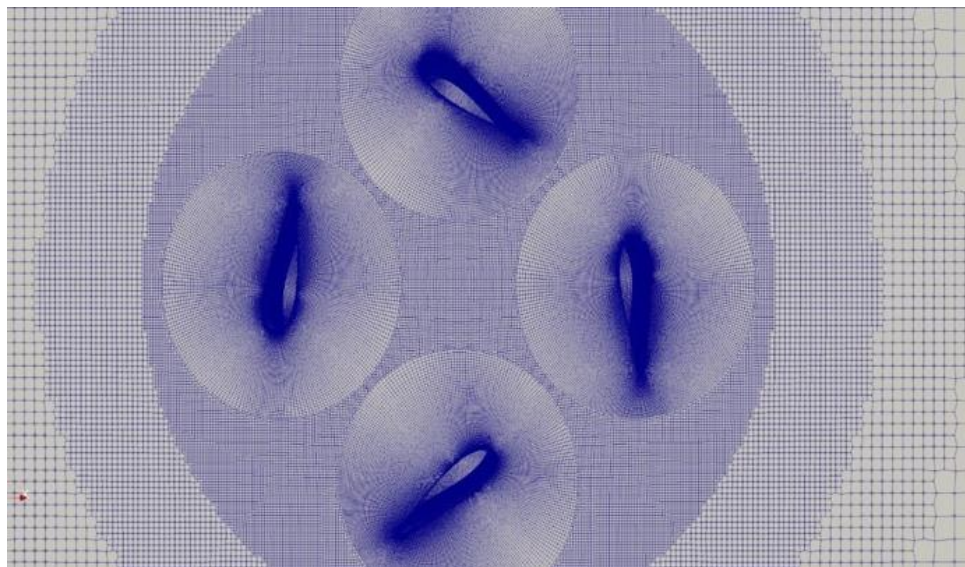


Figure 31 Zoomed view of the mesh with AMI

Table 2 Statistic inspection of mesh

Mesh at Pitching angle	Data Type	No. of Cells	No. of Points	Memory (MB)	Geometry Size (MB)
45	Multiblock Dataset	6154053	3356160	1112.948	110.352
90	Multi-block Dataset	6107608	3236995	1090.64	112.308
135	Multi-block Dataset	5959071	3250438	1078.025	105.105
180	Multi-block Dataset	5281492	2817824	947.537	90.588
225	Multi-block Dataset	5656766	2987188	1010.477	97.701
270	Multi-block Dataset	6108598	3238636	1090.978	112.274
315	Multi-block Dataset	5944126	3240709	1075.081	104.953
345	Multi-block Dataset	5293087	2821693	949.31	90.776

6.4.6 BOUNDARY CONDITIONS:

The boundary conditions are set to specify patch's types and flow properties at the edges of the domains. In the following, the hemispherical far-field will be referred to as far-field, while the airfoil surfaces will be called blades. The patches defining the interpolation interface are called AMI. Table shows the specified boundary conditions for U , p , k , ω and v_t .

	Farfield	Blades	Symmetry	AMI
U	Type pressureInletOutletVelocity value uniform (0 0 0)	Type movingWallVelocity value uniform (0 0 0)	Type symmetry	Type cyclicAMI value uniform (0 0 0)
P	Type totalPressure value uniform 0	Type zeroGradient	Type symmetry	Type cyclicAMI value uniform 0
k	Type inletOutlet inletValue uniform 0.002099 value uniform 0.002099	Type kLowReWallFunction value uniform 0.002099	Type symmetry	Type cyclicAMI value uniform 0.002099
ω	Type inletOutlet inletValue uniform 13.201 value uniform 13.201	Type omegaWallFunction value uniform 13.2019	Type symmetry	Type cyclicAMI value uniform 13.201
ν_t	Type calculated value uniform 0	Type nutLowReWallFunction value uniform 0	Type symmetry	Type cyclicAMI value uniform 0

6.4.7 MOTION OF BLADES

The rotor motion is obtained by rotating the background mesh and AMI-cylinder around the rotor center. The pitch function is applied to each AMI cylinder to achieve oscillation around its center and thus blades pitching Motion. The position of the pitching rod is changed in the function to recreate the change in pitching of the cyclorotor. (Donners, 2022)

6.4.8 SIMULATION

A total of 8 simulations were done varying the pitching angle of the cyclorotor. pimpleFoam was used as a solver. The mesh was refined using refined surfaces. The mesh gets more refined as it gets closer to the solver. Time step of $3.6e-4$ was taken. The cyclorotor is rotating at 1400 RPM. The value of kinematic pressure (p) is obtained which is used to calculate the forces in X and Y direction.

Table 3 Simulation parameters

S.No	Parameters	Values
1	Flow velocity	(0,0,0)
2	Kinematic pressure(m^2/s^2)	0
3	RPM	1400
4	Center of rotation	(0,0,0)
5	Axis of rotation	(0,0,1)
6	Center of rotation (Pitching motion)	(0.1,0,0)
7	Incident velocity of air for each blade	11.17 m/s

6.4.9 POST PROCESSING:

In simulation, post-processing refers to the process of analyzing and interpreting the results of a simulation after it has been completed. This can involve visualizing the results in graphs or plots, calculating statistical measures such as mean and standard deviation, or comparing the results to experimental data or other simulations. The goal of post-processing is to extract meaningful insights and information from the simulation results that can be used to understand the system being simulated and make informed decisions about its design or operation. Here we obtain the values of lift. The steps are:

1. Extracting the surface from the mesh.
2. Generating surface normal.
3. The lift is obtained by multiplying the surface normal with the pressure.

Let

$$n_y = \text{normals along } y$$

$$n_x = \text{normals along } x$$

Then,

$$\text{Force along } x - \text{direction}(F_x) = n_x * p$$

$$\text{Force along } y - \text{direction}(F_y) = n_y * p$$

$$\text{Thrust} = \sqrt{F_x^2 + F_y^2}$$

$$\text{Thrust angle} = \tan^{-1}\left(\frac{F_y}{F_x}\right)$$

The thrust angle is measured with the X-axis as a reference line.

Table 4 Simulation results

Pitching Angle	Force along X axis	Force along Y axis	Resultant thrust	Thrust angle
0	0	112	122	90
45	-79.4667	88.066667	118.61993	132.062
90	-126.8	0	126.8	180
135	-82.53333	-85.6	118.9079943	226.045
180	0	-119.46667	119.466667	270
225	84.93333	-88.3	122.5175951	313.887
270	123.83333	0	123.833333	360
315	89.4	88.466667	125.77457	404.699
360	0	122.03333	122.0333333	450

The graph shown is plotted from the values obtained from simulation done at 8 different pitching angles. The graph obtained by plotting the forces in X and Y direction vs the pitching angle is sinusoidal in nature. We can also see that these two graphs are opposite in nature, i.e., at maximum force in X direction there is min Force at Y direction and vice versa. The resultant of these two forces is found to be almost constant in all 8 simulations at different pitching angles.

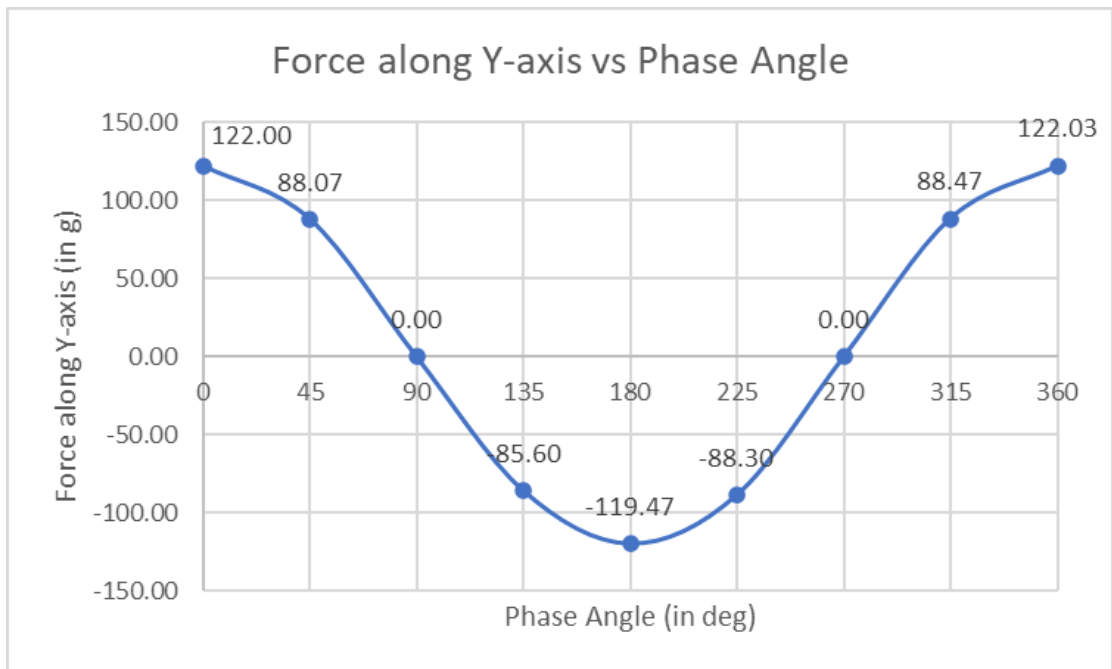


Figure 32 Force along Y-axis vs phase angle curve

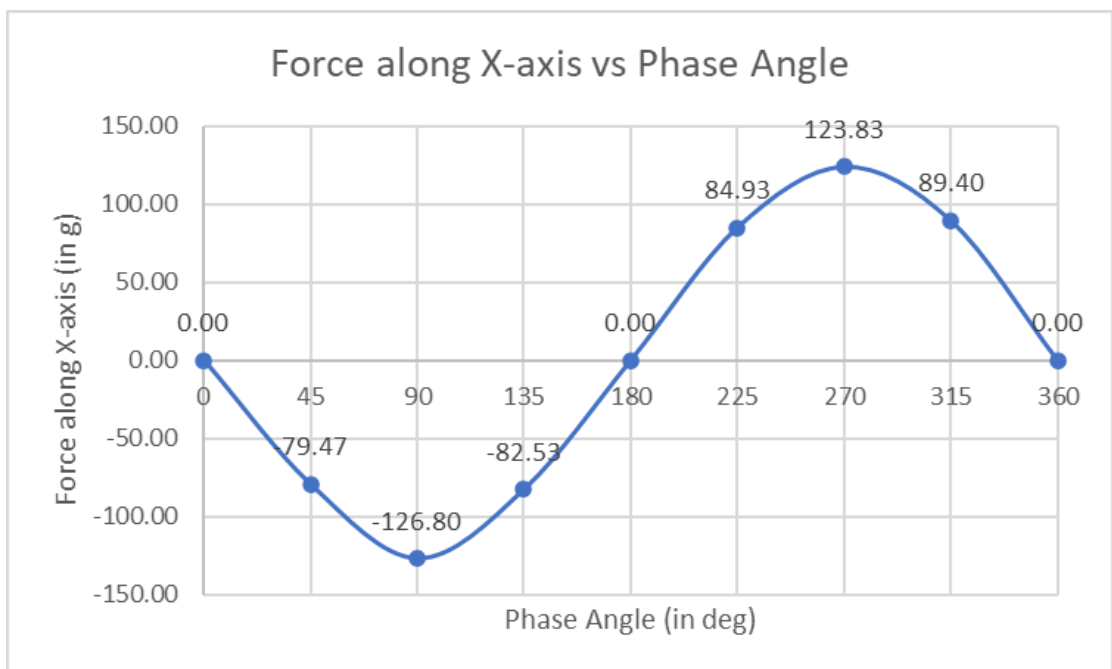


Figure 33 Force along X-axis vs phase angle curve

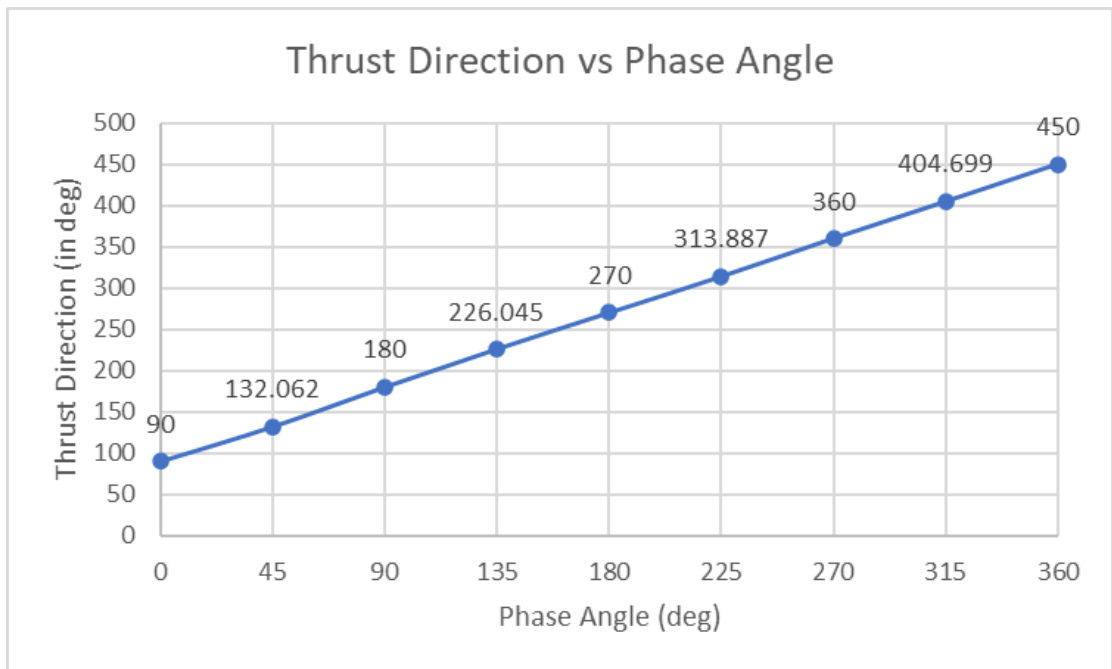


Figure 34 Thrust direction vs phase angle curve.

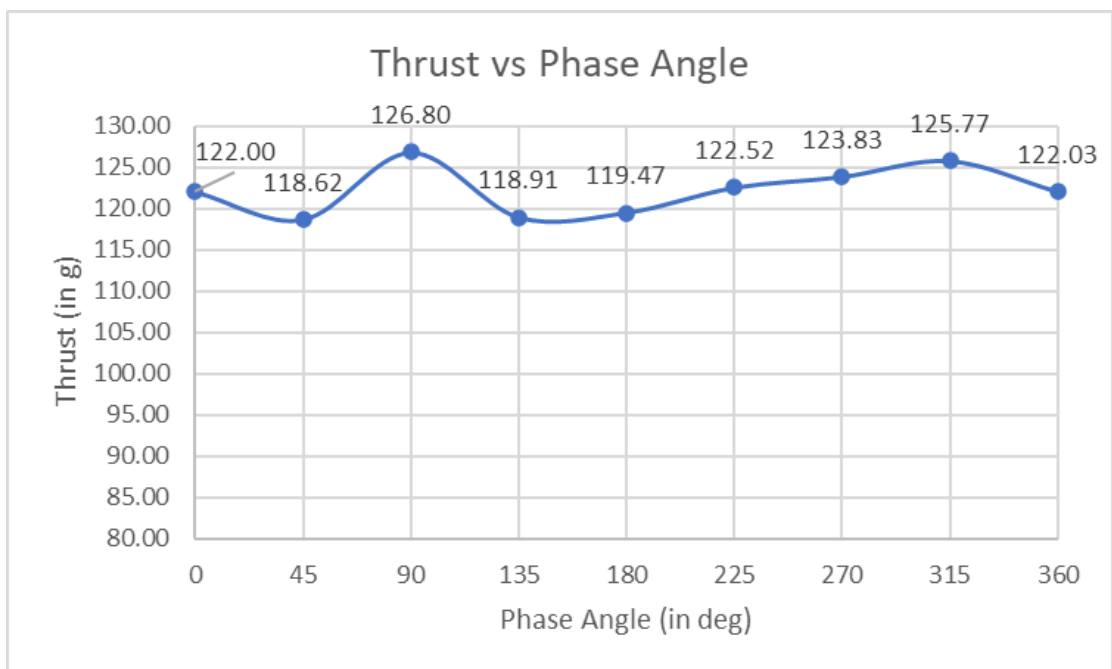


Figure 35 Thrust vs phase angle curve.

CHAPTER SEVEN

MANUFACTURING AND ASSEMBLY

7.1 FABRICATION

7.1.1 CYCLOROTOR

Cyclorotor is a product and hence is an assembly of many parts which are brought together in an organized way such that the product functions as desired by the designer. It is important to have individual parts designed and manufactured to the accuracy so that they fit right on their counterparts or other parts where they are meant to be fitted.

The parts of the cyclorotor are modeled using CATIA software and manufactured using a 3D printing manufacturing process. Below section describes each part of the cyclorotor in detail.

7.1.1.1 MAIN ROTOR WHEEL

Main rotor wheel is the rotating part of the cyclorotor where the blades are attached. The rotor wheel has GT2 gear pulley attached to it concentrically and hence is responsible for receiving the power from the motor and rotating the airfoils to meet its prime objective. The rotor is seated on the main shaft which runs along the full length and beyond the rotor. The rotor is assembled such that it can rotate about the axis of the main shaft. The main shaft fixes the whole rotor to the body of the aircraft.

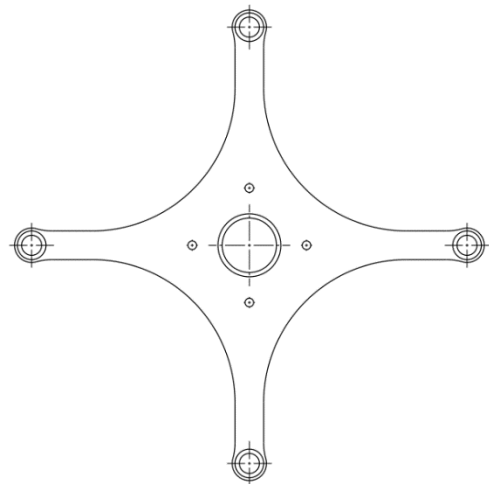


Figure 36 Main rotor wheel

7.1.1.2 AIRFOIL BLADE

Airfoil blade is the extruded form of an airfoil and plays a significant role in cyclorotor as it is responsible for producing desired lift and thrust. A variety of airfoils are

available, however symmetrical airfoils are mostly preferred for use in cyclorotor since the airfoil has to generate lift through both of its faces according to its position around the rotor. This project uses NACA0015 airfoil with chord length of 38.1 mm (1.5 in US metric) and effective span of 152.4 mm. The airfoil is mounted to the main rotor wheel at 25% of the chord from the leading edge such that it can rotate about the axis parallel to the blade and passing through the point. The airfoil also has another point at which force due to the control rod acts. The action of the control rod on the blade allows it to attain a different pitching position when it rotates around the rotor circumference.

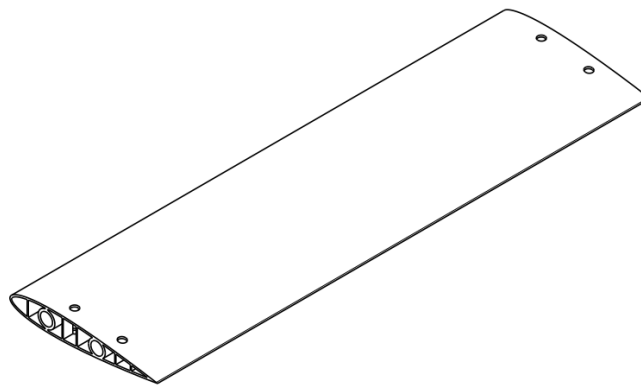


Figure 37 NACA0015 Airfoil blade

7.1.1.3 CARBON ROD SPAR

Carbon rod spar is reinforcement provided to the airfoil blade along with its contribution on assembly of airfoil blade with rotor wheel. It is a circular cross section solid rod which runs along the length of the airfoil blade and extends beyond the length passing through the holes on the edges of the rotor wheel providing assembly of the blade to the rotor wheel. Similarly, another carbon rod runs through the hole on the aft portion of the blade which is dedicated in reinforcement of the blade along with providing actuation point where the control rod can apply force for pitching the blades.

7.1.1.4 CONTROL ROD

Control rod is a link connecting the eccentric point and the blade through the airfoil holder so that the blades' pitching amplitude can be controlled. It extends up to the aft portion of the holder so that the blades can be easily moved. Control rods can be

controlled by controlling the eccentric point which can be again controlled by servo motors. The movement of the eccentric point allows the control rod to pitch the different blades with different amplitudes. The set of control rods is free to rotate about the eccentric point. This control rod mechanism is the only reason for the cyclorotor being able to produce thrust in any direction around 360 arcs.

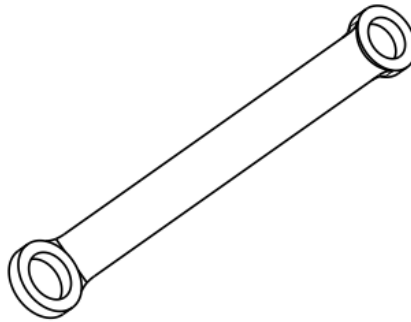


Figure 38 Control rod

7.1.1.5 MAIN ROTOR SEPARATOR SHAFT

Main rotor separator shaft is a hollow cylindrical shaft which joins two main rotor wheels with a constant gap between them. It is important to have a fixed gap between the two rotors for the product to work effectively. More important is that the two rotors should have the same rotational speed and relative speed between them zero. Since only one of the main rotor wheels has a gear pulley attached to it and hence the power from the motor has to be transferred to the other rotor either, for this the main rotor separator shaft comes to action.

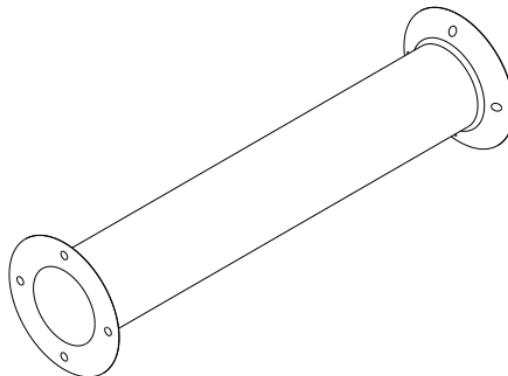


Figure 39 Main rotor separator shaft

7.1.1.6 SERVO-SHAFT COUPLER

Servo-shaft coupler is a coupler which is responsible for movement of the eccentric point which is powered by the servo motor. There are two servo-shaft couplers in this product viz: Servo-shaft Coupler Inboard and Servo-shaft Coupler Outboard. The outboard coupler lies at the other end than where the motor actuation takes place and has an eccentric shaft perturbed through it. It acts as the limiter for the rotor so that the rotor does not slip to the side and gives support to the control-rod wheel to rest on and rotate about. The inboard coupler lies at the end where the motor actuation takes place and again works as the limiter for the rotor. Besides, it also provides a platform for the motor mount to rest on.

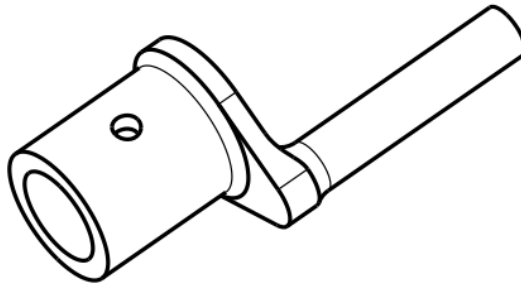


Figure 40 Servo-shaft coupler (Outboard)

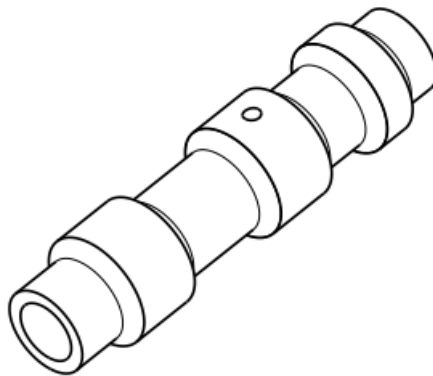


Figure 41 Servo-shaft coupler (Inboard)

7.1.1.7 PULLEY COUPLER

Pulley coupler is an intermediate component between the rotor wheel and the GT2 timing pulley which provides attachment facility to the pulley to the rotor wheel. The GT2 timing pulley cannot be directly bolted to the rotor wheel due to its small dimension, hence an additional coupler which is mate able to the pulley slot is manufactured and employed on the system. The coupler is bolted to the rotor and attaches to the rotor firmly.

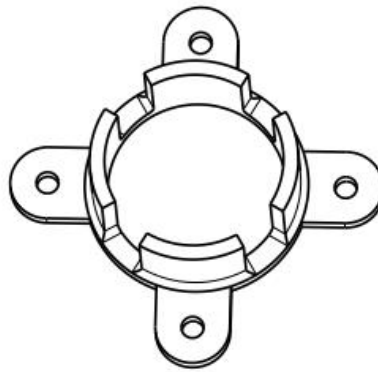


Figure 42 Pulley coupler

7.1.1.8 TIMING PULLEY

Timing pulley is a toothed pulley which is used to transfer power and manipulate torque from one position to another position on the same plane. Two pulleys are used in this product; one with 60 teeth and another with 20 teeth so that the torque multiplication factor is 3. The smaller pulley acts as the driver pulley whereas the bigger pulley acts as the driven pulley. The two pulleys are linked by a GT2 6mm width timing belt.

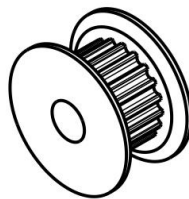


Figure 43 GT2 timing pulley 20 teeth

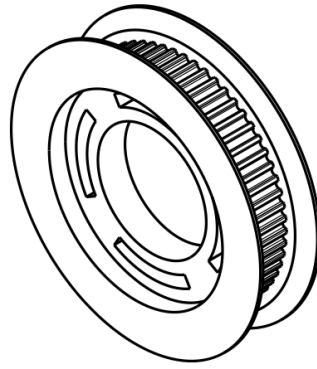


Figure 44 GT2 timing pulley 60 teeth

7.1.2 TEST RIG

Test rig refers to a testing apparatus which is dedicated for measuring the magnitude of thrust generated by the cyclorotor. Our test rig contains a load cell which has a maximum capacity of up to 5kg with the unidirectional feature i.e., it ignores the load applied in the any direction other than stated by the manufacturer.

The strain gauge has been placed on a flat base as prescribed by the manufacturer and then the electronic components are integrated into the structure. The overall system here, the test rig, has a flat surface on the top of the strain gauge where the load is expected to be placed. The upper flat surface plate and lower flat surface plate are linked by strain gauge as shown in *figure 45*. The lower flat surface flat is the substrate which is to be mounted to a rigid flat surface. One end of the strain gauge is fixed to the substrate plate and the other end is the free end where upper flat plate is attached such that when load is put on the upper flat plate the strain gauge gives the output of the load applied.

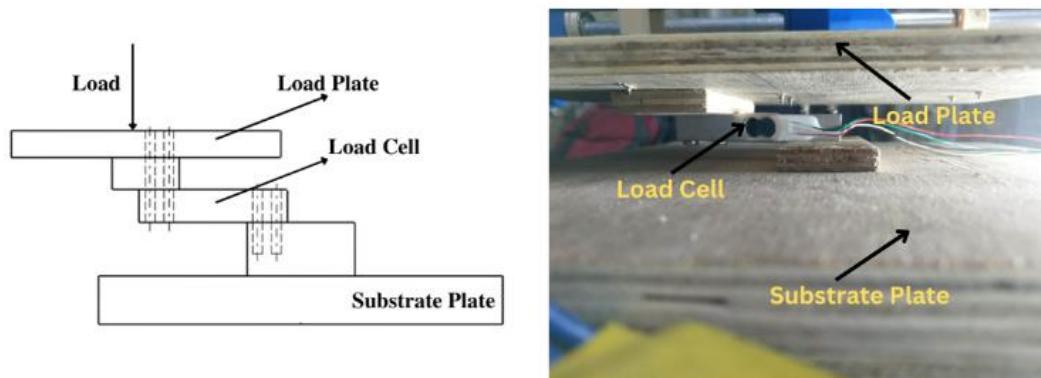


Figure 45 Test rig

The strain gauge is integrated with an HX711 load cell amplifier which is responsible for generating signal output. To fetch the real-time output of the load applied on the strain gauge, an Arduino Uno has been programmed and integrated with the HX711 module. The Arduino Uno here is responsible for sending the commands for calibration of strain gauge through the HX711 module and fetching the signal output of the load applied from the strain gauge. The HX711 library is uploaded to the Arduino first and then the calibration and read test of the strain gauge is carried out. HX711 library offers the interface to communicate with the semiconductor and fetch the data from the strain gauge.

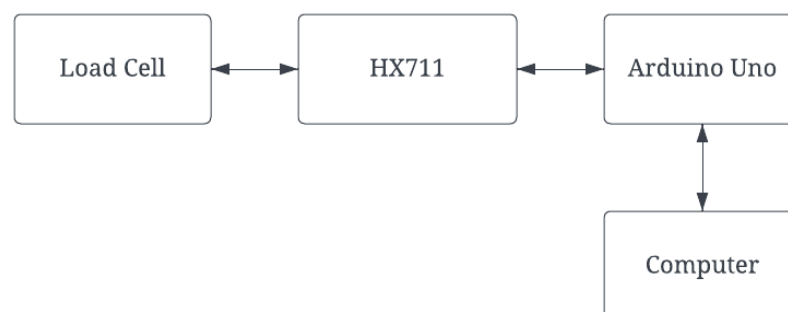


Figure 46 System architecture of test rig

7.2 ASSEMBLY

7.2.1 CYCLOROTOR

The cyclorotor is an assemblage of all the component parts mentioned in the preceding section. All the parts are arranged in a definite manner so that the rotor functions well. Main shaft is the parent part of this product as all other parts are fitted or assembled on this main shaft. The main shaft hence holds the whole rotor on it and fixes the rotor to a rigid substrate. The assembly is such that the main shaft can rotate independently and freely about its axis, also allowing the rotor to rotate independently about the same axis. Although the product seems sophisticated and heavily loaded with parts, its assembly has been simplified using simple joints. The product can be assembled using a set of bolts and nuts of two different sizes only and a set of screws of the same size. Hence, assembly of this product requires only two hand tools viz: screwdriver and plier, no power tool is required.



Figure 47 Assembled product of cyclorotor.

7.2.2 EXPERIMENTAL SETUP

The substrate of the test rig is attached to a rigid table with the help of C-clamps so that the setup is free of vibration due to loose parts. On the upper flat surface, the cyclorotor has been fixed using different mounts. The axis of the main shaft of the cyclorotor has been maintained parallel and aligned to the axis of the strain gauge. The main shaft has a handle assembled to it which has provided the cyclorotor with a facility to be mounted on any flat surface. The cyclorotor fixed to the test rig can be seen from *figure 48*. The mounts are attached to the upper flat surface of the test rig with screws.

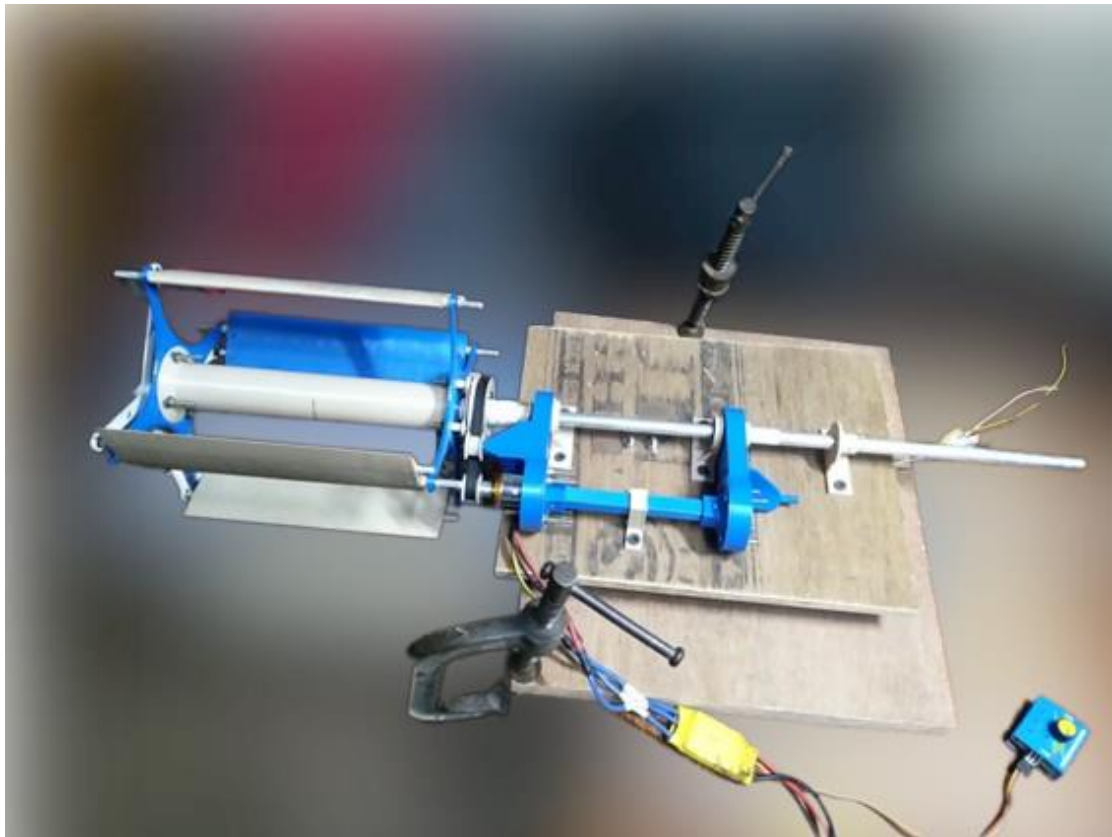


Figure 48 Experimental setup

The experimental setup also involves the electrical connections of the motor to the motor controller and the load cell to the computer. The motor is powered by a 3S LiPo battery. Since the motor is brushless the amplifier module is required for which ESC module has been used and for the control signal generation, servo tester module has been used.

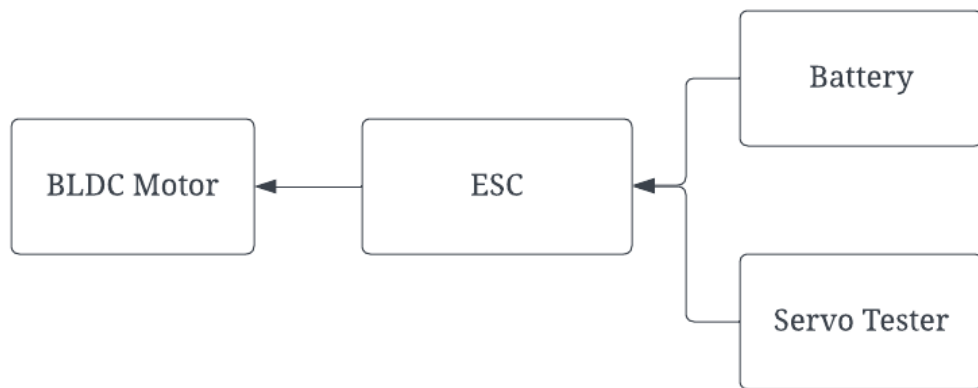


Figure 49 Driveline system architecture

The system architecture for the test rig has been discussed in the preceding section, hence the setup is arranged accordingly. The electrical connections of the system include connection of load cell to HX711 amplifier which is electrically connected to the Arduino and the Arduino is powered and programmed by a computer.

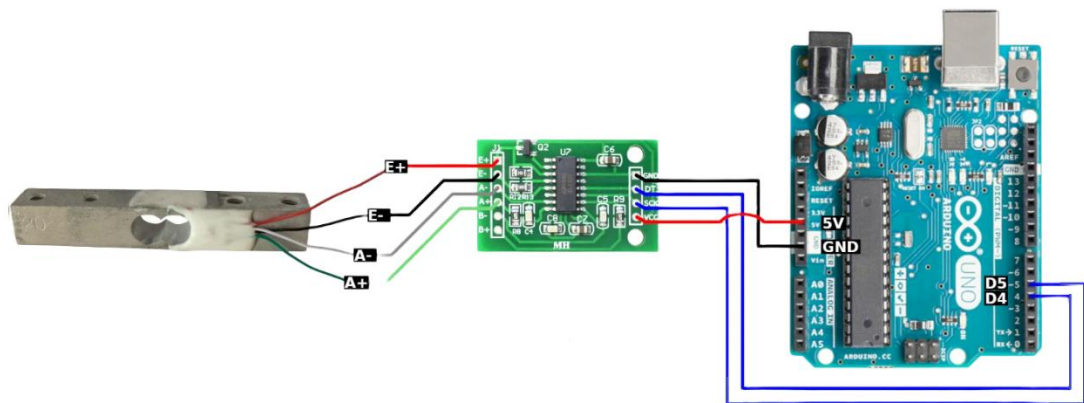


Figure 50 Electrical wiring for test rig

CHAPTER EIGHT

EXPERIMENTATION, RESULT AND DISCUSSION

8.1 EXPERIMENTATION

Experiments of the assembled product are carried out on the dedicated test rig. The experimental setup is assembled as discussed in the preceding section. The setup is fixed to a rigid table in such a way that the cyclorotor portion will overhang and is free from any obstruction. This ensures the undisturbed flow of air to and through the cyclorotor blades. Before the cyclorotor is powered and the experiment is carried out the strain gauge is calibrated using a 280-gram known load. The calibration feature is offered by the HX711 library itself. However, the system needs frequent calibration after a few disturbances have been applied on the test rig so that reliable data can be obtained.

As mentioned in the objective, the main object of this experiment is to obtain a thrust vector pattern in cyclorotor. Since cyclorotor can produce thrust in any direction in a 2D plane, the thrust produced can be resolved in to two components namely horizontal (along X-axis) and vertical (along Y-axis). Hence the experiment is carried out separately for force produced by cyclorotor along Y-axis and X-axis, then later the forces are vector summed for obtaining the resultant thrust magnitude and direction. The coordinate system of the overall all system is the universal coordinate system as shown in *figure 51*. However, the coordinate system for the phase angle is such that the phase angle is at 0° when the eccentric point coincides along the Y-axis and is below the X-axis. The cyclorotor was simulated at 1400 RPM hence the experiment is also carried out at 1400 RPM however due to losses in the drive system the actual rotation speed of the rotor was recorded to be 1343 RPM.

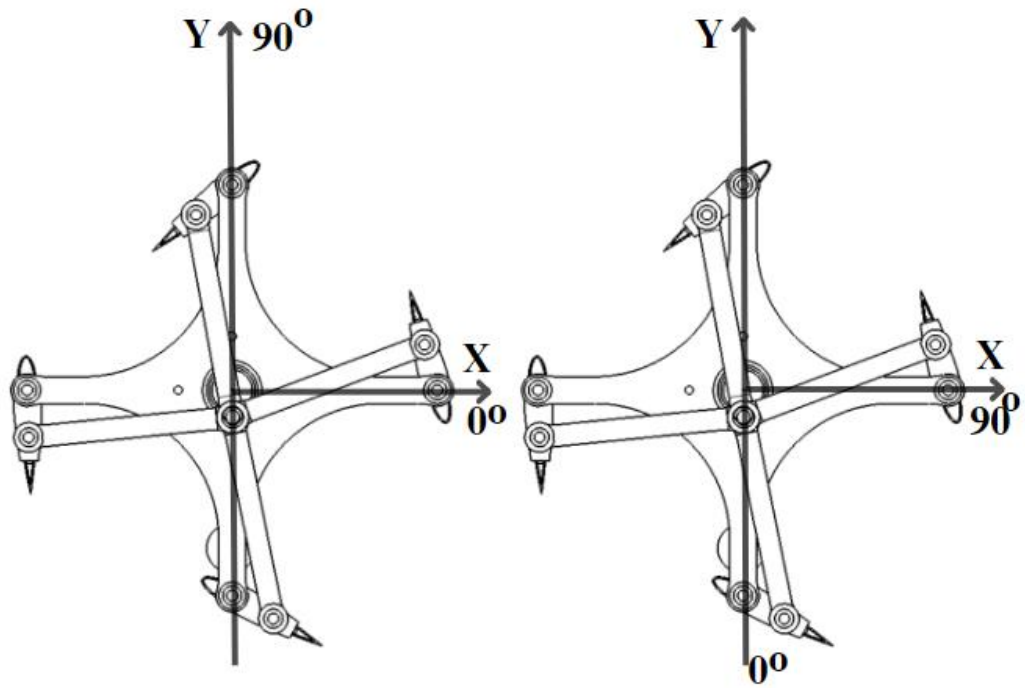


Figure 51 Coordinate system for the whole system (left) coordinate system for phase angle (right)

For force produced along the Y-axis, the above-mentioned experimental setup is used. Cyclorotor is powered through the battery and HX711 is powered through Arduino which in turn is powered by the computer to which it is connected. First the phase angle is set to 0° and increased by 45° to 360° . The RPM of the motor is set so that the rotor's speed is 1400 RPM using the servo tester (measured speed being 1343 RPM). The force produced is recorded by observing from the computer screen which showed the real-time loading of the load cell.

For measurement of the force produced along X-axis, the substrate of the test rig is mounted on a vertical flat surface. Hence the setup is 90° in angle to that of the setup for the Y-axis however the coordinate system is the same as for Y-axis setup. The procedure of carrying out experiment is the same as that for Y-axis. The force produced is noted from the computer screen which shows the real-time loading of the load cell.

8.2 EXPERIMENTAL RESULTS AND DISCUSSION

The experiment was carried out at 1343 RPM with the phase angle varying from 0° to 360° . The force produced was recorded for each orientation i.e., Y-axis and X-axis on every 45° change in phase angle. The results obtained can be seen below in the form of curves.

From *figure 52* the maximum force produced along Y-axis is at the phase angles when the eccentric point coincides with Y-axis. This is because at such positions the two airfoil blades contribute totally to the force generation whereas the other two airfoils remain such that no force is produced on it. The maximum force obtained is at 180° phase angle which shows the force is directed towards the negative Y-axis. This is since gravity assists prevail when the force is directed in the direction of gravity. Hence there is little variation in the force produced which is existence during the experimentation probably caused due to uncontrolled experimental environment and vibrations which persisted on the cyclorotor when it was in operation. The nature of the curve is of sinusoidal type which validates the successful implementation of the sinusoidal low pitch system in our cyclorotor.

From *figure 53* it can be observed that the maximum force produced along the X-axis is at the phase angles when the eccentric point coincides with the X-axis. This is because of the same condition as discussed in the previous case. The maximum force obtained is 104 grams at 270° phase angle which is 2 grams more than 102 grams at 90° phase angle. The deviation in the force probably can be caused due to the vibration that persisted during the operation of the cyclorotor. The nature of the curve obtained is sinusoidal type which validates our successful implementation of low pitch sinusoidal system.

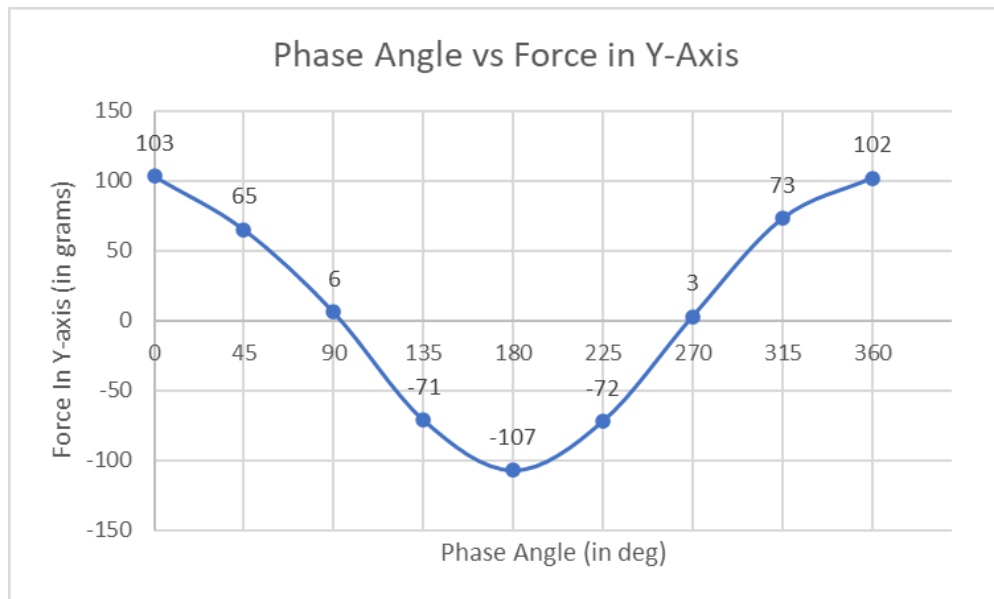


Figure 52 Force along Y-axis vs phase angle curve

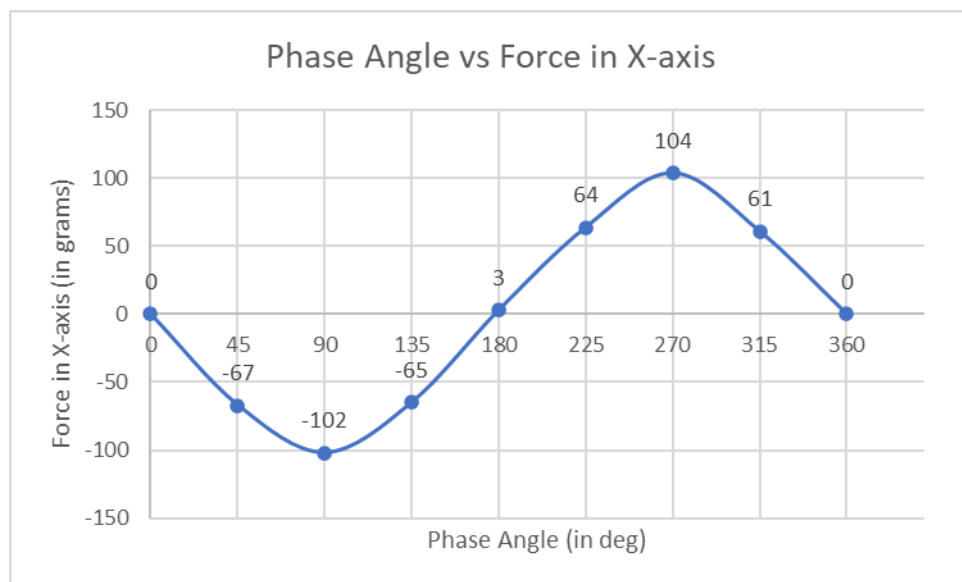


Figure 53 Force in X-axis vs phase angle curve

The resultant thrust was obtained by vector summing the two components of forces obtained from the experiments. **figure 54** shows the thrust magnitude developed by the cyclorotor at different phase angles. It can be seen from the curve that there is variation in thrust generation at different angles. Theoretically the thrust is expected to be constant throughout the phase angles, but experimental results show there is deviation in values at different angles whose reason is not studied in this experiment and can be an issue for further study.

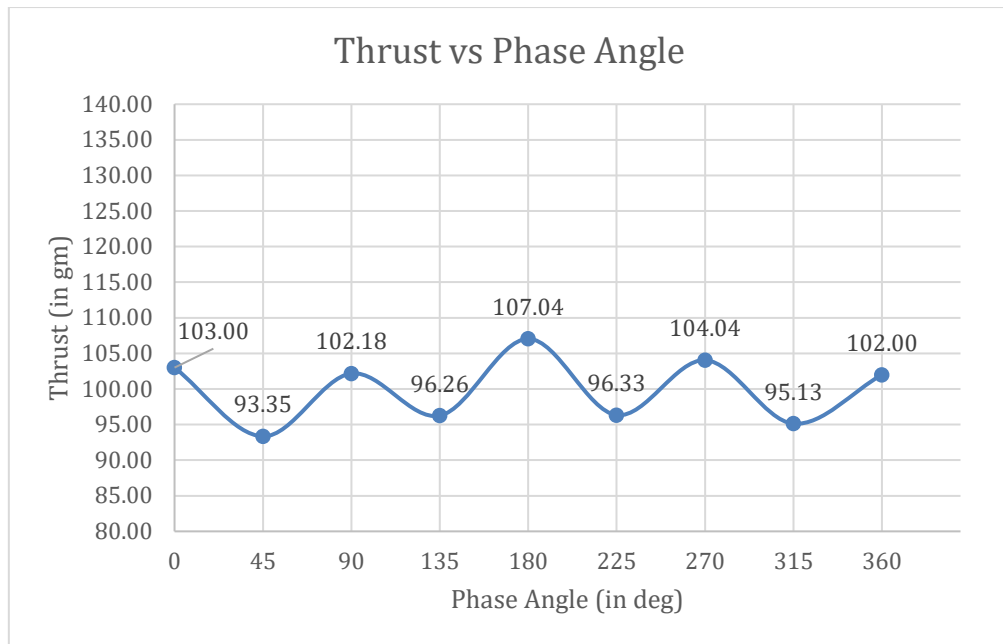


Figure 54 Thrust magnitude vs phase angle curve.

The thrust direction was obtained from the data obtained by using vector algebra. The curve shows approximately linear nature and shows that the thrust direction is nearly opposite to the direction of the eccentric point. Hence the line joining the center of the rotor and the eccentric point at any instant shows the phase angle and the thrust direction at that instant also showing the direction of the phase angle and thrust is opposite to each other.

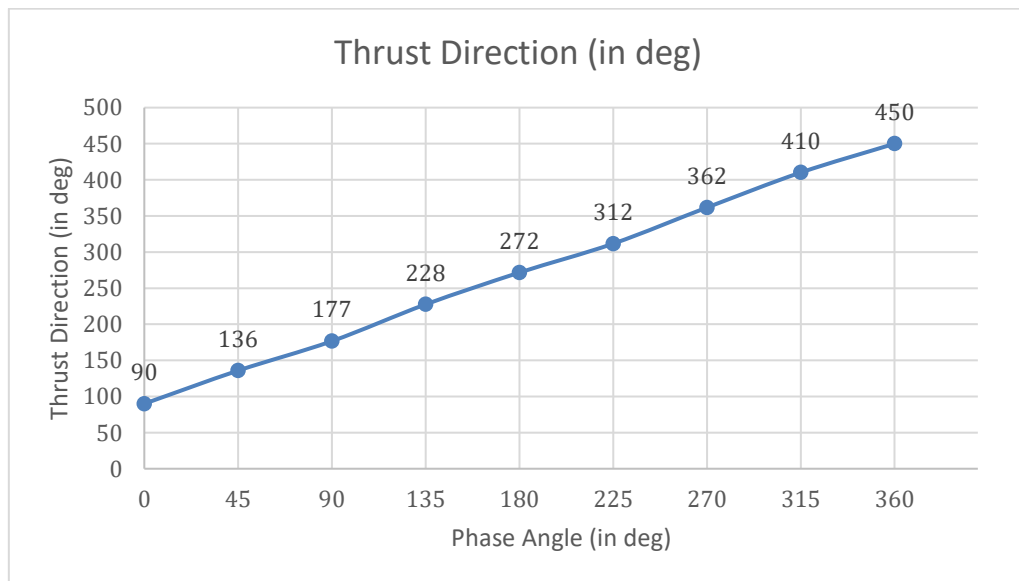


Figure 55 Thrust direction vs phase angle curve.

Comparison of the forces along and Y-axis and X-axis show phase difference of 90° which is due their orientation being 90° different in phase. Similarly, the comparison curve shows that the force magnitude is similar with respect to the phase angle.

Figure 57-58 shows the comparison of experimental and numerical results for the forces along both the axes. Similarly, **figure 59** shows the comparison of experimental and numerical results for the resultant thrust generated by the cyclorotor with respect to the change in phase angle.

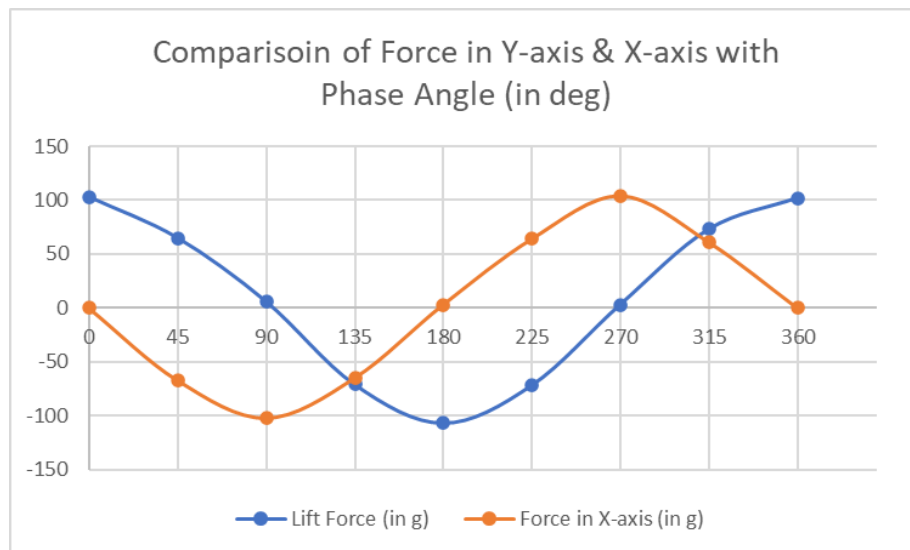


Figure 56 Comparison of force in Y-axis & X-axis with phase angle

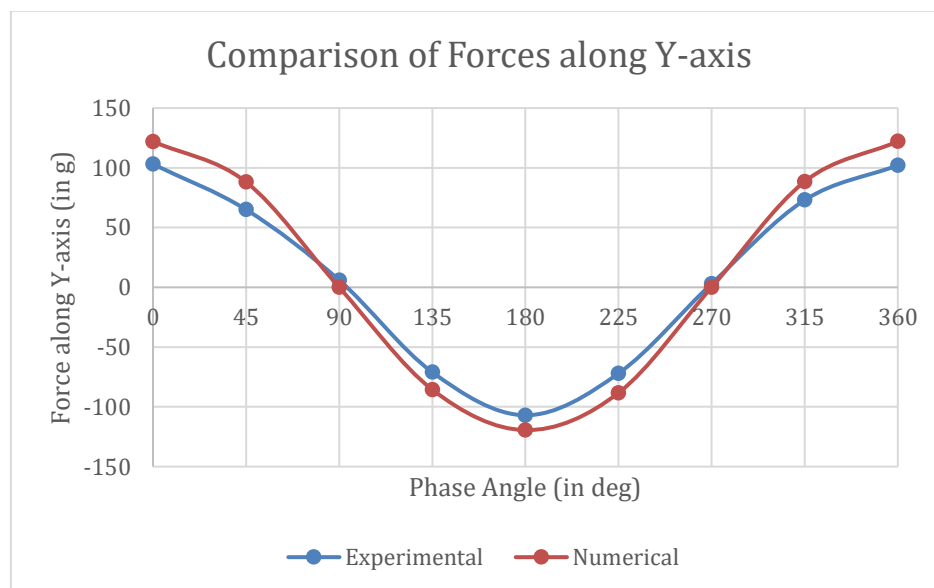


Figure 57 Comparison of experimental and numerical forces along Y-axis



Figure 58 Comparison of experimental and numerical forces along X-axis

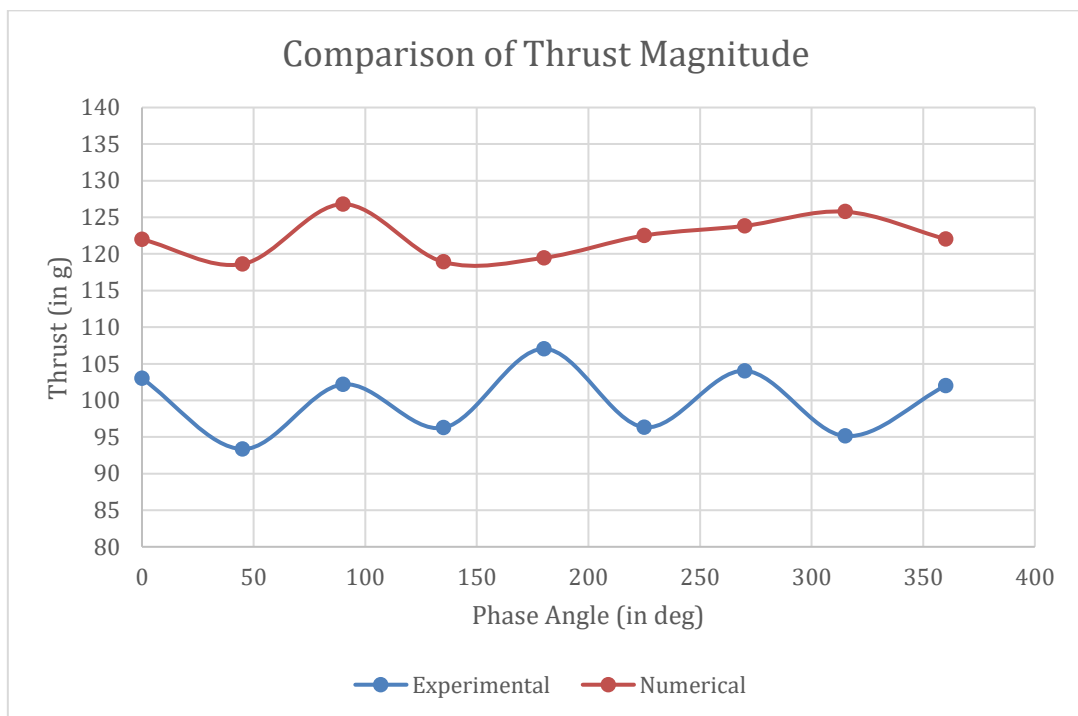


Figure 59 Comparison of experimental and numerical thrust results

CHAPTER NINE

CONCLUSION

This report discusses the experimental parametric study of eccentric phase angle on thrust produced by cyclorotor. The experimental parametric study was conducted using a model cyclorotor with blades of 6-inch span, rotor diameter of 6-inch and eccentric distance of 10 mm. The RPM for the experiment was set to a constant single value of 1400 RPM which in real experiment was recorded to be 1343 RPM. The eccentric distance also remained constant for the entire experiment. The experiment was carried out on a unidirectional thrust measuring stand built for this experiment. Thus, the experiment was carried out for force generated along Y-axis and X-axis separately. The thrust magnitude and direction were obtained through computation and analysis of the experimental results.

Conclusions from the experimental parametric study are:

1. The four-bar pitch mechanism known as sinusoidal low pitch mechanism strictly follows the sinusoidal character which resulted in curve of lift generated for both experiments also to be of cosine nature.
2. The curves obtained from the simulation and the experiments were in close approximation with each other which showed the cyclorotor was able to perform well in terms of character of functionality. Despite the functionality, there persists significant error in magnitude of thrust.
3. The thrust direction curves obtained from both simulation and experiments were comparable and show that the thrust direction is in opposite direction to the eccentric phase angle line.
4. Since the thrust direction is always in opposite direction to the eccentric phase angle line at any instant, vertical flight can be achieved when the eccentric phase angle is at 0° . Similarly, pure forward thrust can be achieved when eccentric phase angle is at 90° . Eccentric phase angle moving from 0° to 90° , the vertical component of the thrust decreases sinusoidally whereas the horizontal component increases sinusoidally.

CHAPTER TEN

PROBLEMS AND LIMITATIONS

10.1 PROBLEMS

All the parts were 3D printed hence some parts which were subjected to high loading failed frequently. The bearings had to be press fitted but due to 3D printing part expansion rate on heating problems rose on fitting. The control rod had to be mounted with the same offset from the airfoil blade and all the control rods could not be mounted on the same location of the servo coupler at the outboard. This obligated us to design specific control rods for each airfoil blade, innermost control rod being less slanted and outermost control rod being most slanted. During the operation of the cyclorotor, at a certain RPM the system vibrated with maximum amplitude due to resonance of the system's natural frequency and rotational speed. This vibration caused the system to fail several times. The simulation was so intense that the computational power and computational time was very high.

10.2 LIMITATIONS OF THE PROJECT

The project being under research and not commercially available was obvious to have limitations on the project.

1. Since no standard dimensions are available for the parts, the part design has some uncertainty.
2. The developed control mechanism has not been released yet by the researchers and experimentalists hence we had to rely on the conventional control mechanism.
3. The vibration due to resonance with the system's natural frequency caused limitation to the RPM of the cyclorotor.
4. The model being small, parts assembly involved inefficient joints which caused inefficient functioning which caused deviations in results.
5. Due to high computational power and computational time the meshing could not be refined as expected.

REFERENCES

1. Arndt, R. (n.d.). *Rohrbach Cyclogyro*. Retrieved June 25, 2022, from [discaircraft.greyfalcon.us:](http://discaircraft.greyfalcon.us/)
<http://discaircraft.greyfalcon.us/Rohrbach%20Cyclogyro.htm>
2. Benedict, M., Chopra, I., & Gupta, R. (2013). Design, Development and Open-Loop Flight-Testig of a Twin-Rotot Cyclocopter. *Journal of the American Helicopter Society*, 58, 1-10. doi:10.4050/jahs.58.042005
3. Benedict, M., Jarugumilli, T., & Chopra, I. (2013). Effect of Rotor Geometry and Blade Kinematics on Cycloidal Rotor Hover Performance. *Journal of Aircraft*, 50, 1340-1352. doi:10.2514/1.C031461
4. Benedict, M., Joseph, M., Chopra, I., & Gupta, R. (2016). Development of a Quad Cycloidal-Rotor Unmanned Aerial Vehicle. *Journal of the American Helicopter Society*, 61(2), 1-12. doi:10.4050/jahs.61.022005
5. Blain, L. (2021, June 10). *Russian has flown prototype of its six-seat hybrid VTOL Cyclocar*. Retrieved June 25, 2022, from [newatlas.com:](https://newatlas.com/aircraft/russia-cyclocar-evtol-prototype-flight)
<https://newatlas.com/aircraft/russia-cyclocar-evtol-prototype-flight>
6. Boschma, J. (1998, November). Cycloidal Propulsion for UAV VTOL Applications. *SBIR Topic Number N98-022*, 60. Bosh Aerospace, Inc.
7. Bowers, P. M. (2013, June 8). *ROTOPLAN*. Retrieved June 25, 2022, from [rotoplan.narod.ru:](http://www.rotoplan.narod.ru/) http://www.rotoplan.narod.ru/history_e.htm
8. Chopra, I., Parsons, E., & Sirohi, J. (2007, July 1). Hover Performance of a Cycloidal Rotor for a Micro Air Vehicle. *Journal of the American Helicopter Society*, 52(17), 263-279. doi: <https://doi.org/10.4050/JAHS.52.263>
9. Cogan, S., & Gagnon, L. (2022). Numerical Analysis of Cyclorotor Aerodynamic Properties in Hovering State. *Material Science and Engineering Conference Series*, 1226, p. 012039. doi:10.1088/1757-899X/1226/1/012039

10. *CycloTech Home - CycloTech Revolution of motion*. (2021). (CycloTech GmbH) Retrieved June 25, 2022, from cyclotech.at: <https://www.cyclotech.at/>
11. Donners, L. (2022). *Experimental validation of a cycloidal rotor URANS CFD model and geometric parameter optimization*. Stuttgart: Abschlussarbeit .
12. Gagno, L., Morandini, M., & Fournier, S. (2021, March 22). Parametric Optimization of a Cyclogiro Aircraft Design for Efficient Hover with Aeroelastic Considerations. *Journal of Applied and Computational Mechanics*, 7, 1774-1787. doi:10.22055/JACM.2021.35872.2752
13. Greenshields, C. (2018). *OpenFOAM user guide Version 6*. The OpenFOAM foundation.
14. Greenshields, C. J. (2018). *OpenFOAM user guide Version 6*. OpenFOAM.
15. Holzmann, T. (2018, August 27). *openfoamwiki*. Retrieved from Openfoamwiki:
https://openfoamwiki.net/index.php/OpenFOAM_guide/The_PIMPLE_algorithm_in_OpenFOAM
16. Holzmann, T. (2019). *Mathematics, numerics, derivations and OpenFOAM®*. Leoben, Germany: Holzmann CFD.
17. Hrishikeshavan, V., Benedict, M., & Chopra, I. (2014, April 29). Identification of Flight Dynamics of a Cyclocopter Micro Air Vehicle in Hover. *Journal of Aircraft*, 52. doi:10.2514/1.C032633
18. HU, Y., FU, X., ZHANG, H., WANG, G., & FARHAT, H. (2019). Effects of Blade Aspect Ratio and Taper Ratio on Hovering Performance of Cycloidal Rotor with Large Blade Pitching Amplitude. *Chinese Journal of Aeronautics*, 32(5), 1121-1135. doi:10.1016/j.cja.2019.01.015
19. Jarugumilli, T., Chopra, I., & Benedict, M. (2011, January). Experimental Optimization and Performance Analysis of a MAV Scale Cycloidal Rotor. *49th AIAA Aerospace Sciences Meeting Including the New Horizons Forum and*

- Aerospace Exposition* (pp. 2011-821). American Institute of Aeronautics and Astronautics. doi:10.2514/6.2011-821
20. Jonathan Edward Caldwell - Wikipedia. (2022, May 24). Retrieved June 25, 2022, from en.wikipedia.org: https://en.wikipedia.org/wiki/Jonathan_Edward_Caldwell
 21. Kirsten, F. K. (1928). Cycloidal Propulsion Applied to Aircraft. *Transactions of the American Society of Mechanical Engineers*. 50. American Helicopter Society International.
 22. Lee, H. Y., Jung, J. S., & Hwang, I. S. (2004). A New VTOL UAV Cyclocopter with Cycloidal Blades System. *American Helicopter Society; 60th annual forum proceedings*. 60, pp. 1569-1586. Baltimore: American Helicopter Society International.
 23. Leger, J. A., Pascoa, J. C., & Xisto, C. M. (2015). Analytical Modeling of a Cyclorotor in Hover State. *Proceedings of the Institution of Mechanical Engineers, Part G: Journal of Aerospace Engineering*. 229, pp. 2163-2177. October: SAGE. doi:10.1177/0954410015569285
 24. Leishman, G. J. (2006). *Principles of Helicopter Aerodynamics with CD Extra*. Cambridge University Press.
 25. McMichael, J. M., & S. Francis, C. (1997, Jul). Micro Air Vehicles - Toward a New Dimension in Flight. *U.S Department of Defense Weapon Systems Technology Information Analysis Center (WSTIAC)*, 1. USA.
 26. McNabb, M. L. (2001). *Development of a Cycloidal Propulsion Computer Model and Comparison with Experiment*.
 27. Shrestha, E., Benedict, M., Hrishikeshavan, V., & Yeo, D. (2014). Development of Control Strategies and Flight Testing of a Twing-Cyclocopter in Forward Flight. *American Helicopter Society 70th Annual Forum*. 3. Montreal: American Helicopter Society International.

28. Shrestha, E., Yeo, D., Benedict, M., & Chopra, I. (2017). Development of a Meo-Scale Cycloidal-Rotor Aircraft for Micro Air Vehicle Application. *International Journal of Micro Air Vehicles*, 9(3), 218-231. doi:10.1177/1756829317702048

29. SimScale. (2020, November 5). *CFD:Pimple Algorithm*. Retrieved from simScale: <https://www.simscale.com/forum/t/cfd-pimple-algorithm/81418>

30. Strandgren, C. B. (1933). *THE THEORY OF THE STRANDGREN CYCLOGIRO*. Case File, NATIONAL ADVISORY COMMITTEE FOR AERONAUTICS, Washington. Retrieved June 25, 2022, from <https://ntrs.nasa.gov/citations/19930094690>

31. Wheatley, J. B. (1934, April). Choice of Airfoils for Rotating Wing Aircraft. *Journal of the Aeronautical Sciences*, 1(2), 88-90.

32. Wheatley, J. B. (1934, April). Rotating-wing Aircraft Compared to Conventional Airplanes. *SAE Journal*, 34-35, 115-116.

33. YUN, C. Y., PARK, I. K., HWANG, I. S., & KIM, S. J. (2005, December 1). Thrust Control Mechaism of VTOL UAV Cyclocopter with Cycloidal Blades System. *JOURNAL OF INTELLIGENT MATERIAL SYSTEMS AND STRUCTURES*, 16(11-12), 937-943. doi:10.1177/1045389X05057520

APPENDICES

APPENDIX A: SUPPORTING TABLES / CHARTS

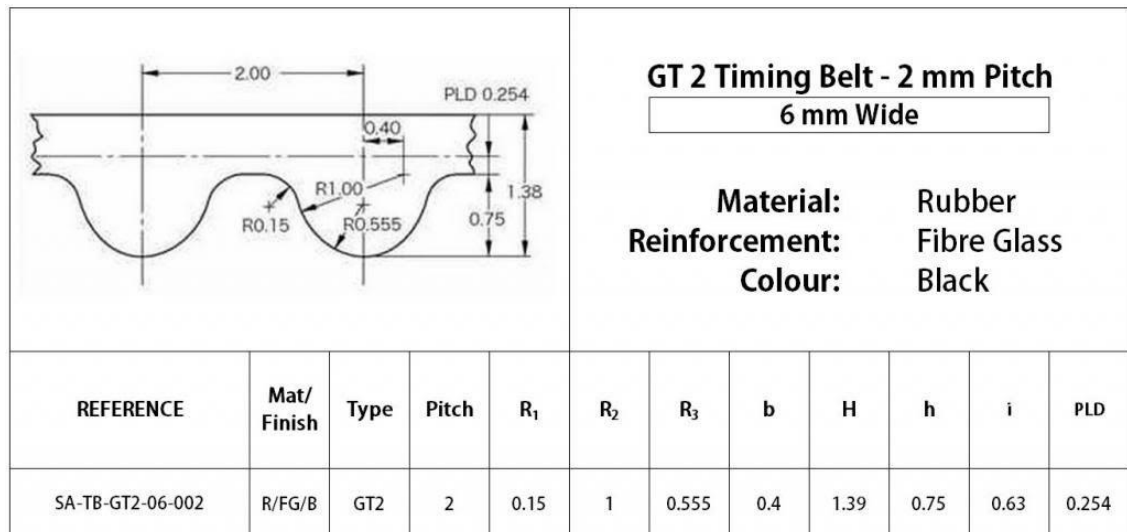


Figure 60 Design Specification of GT2 Tooth Profile (Source: *Mechanica – GT2 Tandriem en Pulley*)

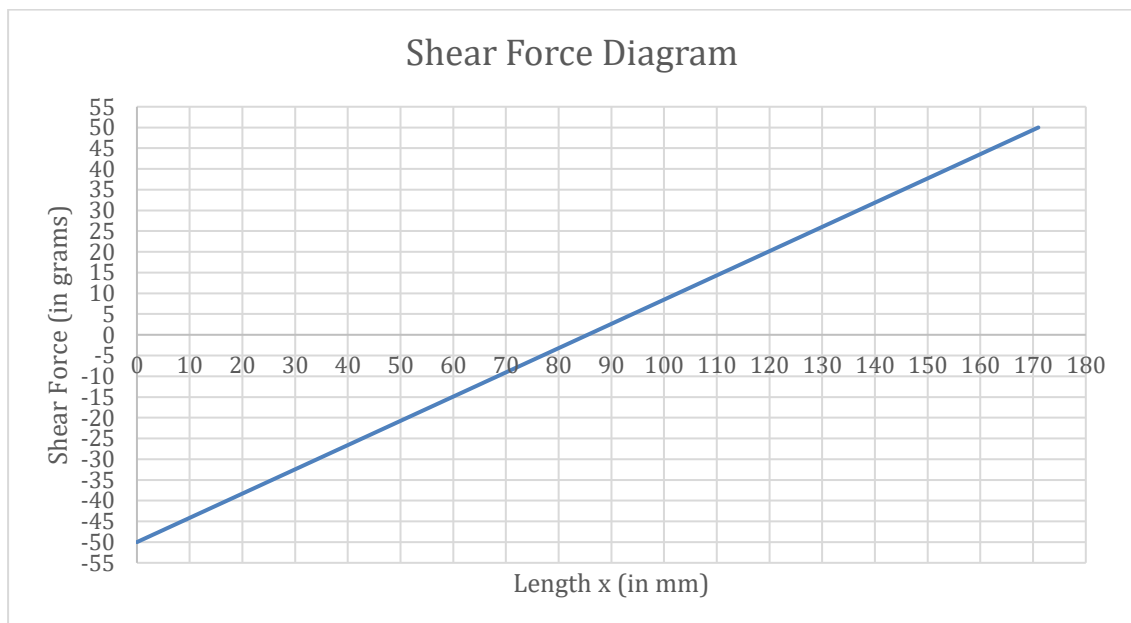


Figure 61 Shear Force Diagram

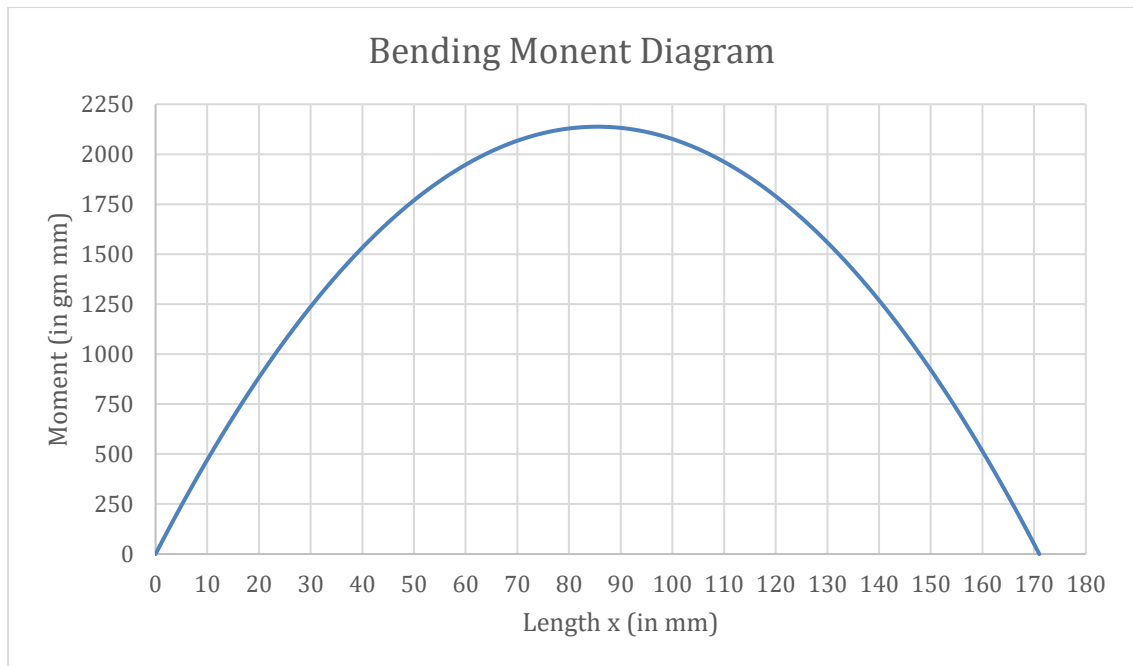


Figure 62 Bending Moment Diagram

Table 5 GT2 Timing Belt Specification (*Source:*
<https://www.himalayansolution.com/product/200-2gt-6mm-belt>)

GT2 Timing Belt Specification	
Breaking Strength	86 N/mm belt width
Temperature Range	-34°C to +85°C
Working Tension	111N for 25.4 mm belt

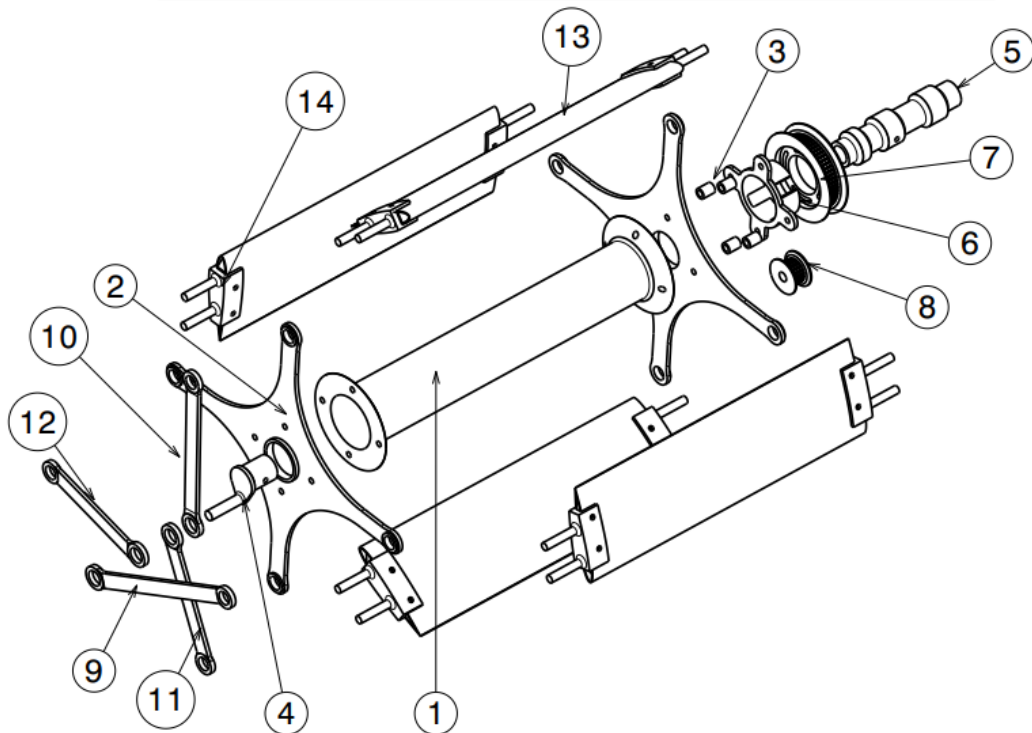
Table 6 Carbon Fiber Properties (Source: <https://goodwinds.com/technical-material-specifications/>)

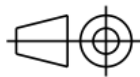
Carbon Fiber Minimum Properties	
Tensile Stress	1.72 GPa
Tensile Modulus	138 GPa
Ultimate Shear Strength	41.3 MPa
Ultimate Tensile Strain	1.50 %
Flexural Strength	1.83 Gpa
Flexural Modulus	131 GPa
Density	1.5 g/cm ³

APPENDIX B: DRAFTING

Bill of Material: Cyclorotor

Part No.	Part Name	Quantity
1	Main Separator Shaft	1
2	Rotor Main Wheel	2
3	Pulley Separator	4
4	Servo Coupler (outboard)	1
5	Servo Coupler (inboard)	1
6	Gear Coupler	1
7	GT2 60T Timing Pulley	1
8	GT2 20T Timing Pulley	1
9	Control Rod 4	1
10	Control Rod 1	1
11	Control Rod 2	1
12	Control Rod 3	1
13	Airfoil Blade (2in)	4
13	Airfoil Holder (2in)	8



PROJECT TITLE: DESIGN AND DEVELOPMENT OF CYCLOTOROTOR FOR PARAMETRIC STUDY OF THRUST VECTOR			
DRAWING TITLE: ASSEMBLY OF CYCLOTOROTOR			
SCALE	1:3	DRG. SHEET NO.	1/1
THAPATHALI CAMPUS, IOE,TU			
Dimensions are in Metric System			

APPENDIX C: PROJECT BUDGET

S.No	Item Name	Quantity	Amount (NRs)
1	PLA Filament	2	7500
2	Aluminum Tube	2	2200
3	GT2 Timing Belt 6mm Width	2	550
4	1400 KV Brushless DC Motor	1	1500
5	Electronic Speed Controller 30A	1	1200
6	Lithium Polymer Battery 2200 mAh	1	4500
7	Servo Tester	1	550
8	Steel Bolts & Nuts M3 x 40mm	40	300
9	Stainless Steel M3.5 x 50mm Bolt & Nuts	40	760
10	Carbon Rob 4mm x 1000mm	2	3500
11	Load Cell	1	750
12	HX711 Moudle	1	500
13	Arduino Uno	1	1500
14	SMB Bearings MR74zz, MR689	64	5000
15	Test Rig Base Plates	2	750
16	Electrical wires and headers	-	1200
17	Miscellaneous	-	5000
Total			37,260

APPENDIX D: PHOTOGRAPHS

